

## Response to Reviewer #1

The authors would like to thank Reviewer 1 for the thoughtful comments and constructive suggestions about investigating further into the main uncertainties in the inversion process and adjusting the constraints on the inversion.

The discrepancies between the base model and satellite retrieved NO<sub>2</sub> columns arise primarily because of the lower modeled than observed NO<sub>2</sub> in rural areas. As noted in the review by Streets et al. (2013), wider spreads between urban and rural NO<sub>2</sub> in models than in satellite observations have been reported in other studies. We note in Section 3.3 our methods of alleviating such discrepancies by adjusting the OH+NO<sub>2</sub> reaction rate and correcting CAMx's low bias for upper tropospheric NO<sub>2</sub> based on the findings of earlier studies. However, additional model shortcomings likely remain (ENVIRON, 2013). In addition, while the NASA OMI NO<sub>2</sub> product, version 2.1, used in this study is the latest available retrieval, it does have some errors that vary spatially and temporally (Lamsal et al., 2014) and retrieval algorithms continue to be refined. It is beyond the scope of this study to fully diagnose or correct all the causes of uncertainties and discrepancies, and to quantify the possible errors in the retrieval processes over our modeling domain.

We have analyzed the influence on the region-based inversion caused by each of the adjustments we made either to the OMI retrieval product or the CAMx a priori simulations (Table R1). It shows that, in this case, missing emission sources (lightning, aviation and soil NO<sub>x</sub> emissions) had the largest effect on the inversion results, especially in rural areas. Using the updated OMI product (with higher resolution) had the second largest effect on the inversion results. Since the new OMI NO<sub>2</sub> narrowed the urban-rural spread, the adjustments over most urban areas and rural areas decrease. The adjustments made in the CAMx model such as decreasing the OH+NO<sub>2</sub> reaction rate and adding an artificial NO<sub>2</sub> layer in the upper troposphere had smaller effects on the inversion results compared to the other changes (Table R1).

The seven inversion regions, five urban regions encompassed by two large rural regions, were carefully designed using sensitivity simulations to ensure NO<sub>x</sub> emissions in each inversion region is mostly responsible for its NO<sub>2</sub> concentrations (Tang et al., 2013). In addition, the five urban regions were chosen to correspond to the urban ozone control regions that are relevant for regulatory attainment and emission control efforts in Texas SIP. The number of source categories is limited by the categorization of emissions in the TCEQ emission inventory. Visual inspection and pseudo-data testing of the categorized emissions were conducted to ensure that the source categories had sufficiently distinct spatial patterns to enable the Kalman filter to distinguish among the sources.

**Table R1.** Scaling factors for NO<sub>x</sub> emissions in each region under alternate inversion cases.

Region-based inversion					
Emission region	Scaling factor (unitless)				
	Missing emission sources <sup>a</sup>	W/ additional emission sources <sup>b</sup>	Using updated OMI product <sup>c</sup>	Decreasing OH+NO <sub>2</sub> rate <sup>d</sup>	Adding a 40ppt layer <sup>e</sup>
HGB	1.31	1.03	1.21	1.18	1.11
DFW	1.32	1.14	1.04	0.98	0.97
BPA	1.90	1.75	1.70	1.72	1.49
NE Texas	1.40	0.56	1.12	1.20	1.10
Austin and San Antonio	1.90	1.70	1.21	1.24	1.15
N rural	2.88	1.98	1.45	1.48	1.24
S rural	3.84	1.72	1.25	1.15	0.98

- Inversion conducted based on OMI v.2.1 and a priori simulation using base case NO<sub>x</sub> emissions; adopted from Tang et al. (2013).
- Inversion conducted based on OMI v.2.1 and a priori simulation using base case with added lightning and aviation and doubled soil NO<sub>x</sub> emissions; adopted from Tang et al. (2013).
- Inversion conducted based on updated OMI v.2.1 (using an a priori NO<sub>2</sub> profile generated from nested GEOS-Chem simulations with a 2005 emission inventory) and a priori simulation with NO<sub>x</sub> emissions from b.
- Inversion conducted based on updated OMI v.2.1 and a priori simulation with NO<sub>x</sub> emissions from b and decreased OH+NO<sub>2</sub> reaction rate.
- Inversion conducted based on updated OMI v.2.1 and a priori simulation from d with an added 40ppt layer in the upper troposphere.

Following are our responses to each of the reviewer's general and specific comments (shown in italics):

General comments:

*1. Both region-based and sector-based NO<sub>x</sub> emission adjustments were made in the paper, but only "sector-based" approach is mentioned in the abstract.*

A sentence "The region-based DKF inversion suggests increasing NO<sub>x</sub> emissions in most regions, deteriorating the model performance in predicting ground-level NO<sub>2</sub> and O<sub>3</sub>" was added to the abstract.

*2. In the Introduction section, more references should be added when discussing "studies using satellite NO<sub>2</sub> measurements to create top-down NO<sub>x</sub> emissions for atmospheric modeling".*

References to Martin et al., (2003); Müller and Stavrou, (2005); Jaeglé et al., (2005); Lin et al., (2010); Konovalov et al., (2006, 2008); Napelenok et al., (2008); Kurokawa et al., (2009); Zhao and Wang, (2009); Chai et al., (2009); and Zyrichidou et al., (2015) were added to the Introduction and Reference sections.

Specific comments:

*1. Please check equation 5 (last term).*

The last term is correct, because we need to consider the difference between prediction and observation at each iteration. The term "S<sub>x</sub>" reflects adjustments after each iteration.

*2. Page 24491, line 23, "while it adds 50% ...": Should it be 49% ?*  
We have changed the number to 49% in the sentence.

3. Page 24493, line 16, "0.09 reduction in both modeled NMB ...": Is it 0.09 reduction in NMB? Table 5 shows that it is from 0.09 to -0.02.

We have changed the sentence to "The model performance is also improved compared against P-3 measurements. For NO<sub>2</sub>, NMB is reduced from 0.09 to -0.02, and NME is reduced by 0.09. For NO<sub>y</sub>, NMB is reduced by 0.16 and NME is reduced by 0.11 (Table 5)."

4. Table 3: Are the "overall" evaluation statistics based on the data from all regions listed above them? Then, the "overall" numbers do not seem to be right. The values should fall between the minimums and the maximums of the separate regions. For instance, in the last column, the NMEs are all above or equal to 0.30, but the overall NME is shown as 0.16.

We double checked the numbers, and they are correct. The "overall" statistics are calculated based on data from all inversion regions, including two large rural regions that encompass the five urban regions presented in the tables. The OMI observations cover each grid cell, and thus the two large rural regions influence the overall statistics in Table 3. For Tables 4 and 6, there are few observation sites outside the five urban regions, making the overall values more similar to the urban values.

## References

- Lamsal, L. N., Krotkov, N. A., Celarier, E. A., Swartz, W. H., Pickering, K. E., Bucsela, E. J., Martin, R. V., Philip, S., Irie, H., Cede, A., Herman, J., Weinheimer, A., Szykman, J. J., and Knepp, T. N.: Evaluation of OMI operational standard NO<sub>2</sub> column retrievals using in situ and surface-based NO<sub>2</sub> observations. Atmos. Chem. Phys. Discuss., 14, 14519–14573, 2014.
- ENVIRON. Continuation on Use of Satellite Nitrogen Dioxide (NO<sub>2</sub>) Data. Final Report to the Texas Commission on Environmental Quality. ENVIRON International Corporation, Novato, CA, 2013.
- Streets, D. G., Canty, T., Carmichael, G. R., de Foy, B., Dickerson, R. R., Duncan, B. N., Edwards, D. P., Haynes, J. A., Henze, D. K., Houyoux, M. R., Jacob, D. J., Krotkov, N. A., Lamsal, L. N., Liu, Y., Lu, Z-F., Martin, R. V., Pfister, G. G., Pinder, R. W., Salawitch, R. J., and Wecht, K. J.: Emissions estimation from satellite retrievals: A review of current capability. Atmos. Environ., 77, 1011–1042, 2013.

1 Tang, W., Cohan, D. S., Lamsal, L.N., Xiao, X., and Zhou, W.: Inverse modeling of  
2 Texas NO<sub>x</sub> emissions using space-based and ground-based NO<sub>2</sub> observations. Atmos. Chem.  
3 Phys., 13, 11005-11018, 2013.  
4

## 5 6 **Response to Reviewer #2**

7  
8 The authors would like to thank Reviewer 2 for the thoughtful comments and description of this  
9 paper as well written and as interesting to the regional air quality community.

10  
11 Following are our responses to each of the reviewer's general and specific comments (shown in  
12 italics):

13  
14 General comments:

15  
16 *1. My concern with using GOES cloud fractions to adjust photolysis rates in the model is that it*  
17 *introduces an inconsistency with the modeled dynamics. Changing the cloud fraction directly*  
18 *affects the heat flux and therefore stability and the height of the boundary layer, both*  
19 *important drivers of ground level O<sub>3</sub>. I understand that it may take considerable effort to*  
20 *fully include satellite-observed cloud fractions in the chemistry and meteorological models.*  
21 *However, I think the authors should at least include a broader discussion of this topic and*  
22 *frame this analysis as a sensitivity study.*  
23

24 We agree with the reviewer on this point. The model dynamic and aqueous phase chemistry  
25 haven't been adjusted by the GOES cloud fractions, and thus are inconsistent with the GOES-  
26 based photolysis rates. This work represents a sensitivity study of the impact of satellite-based  
27 photolysis rates but not a complete assimilation of satellite-based clouds. We have more fully  
28 discussed this limitation in the conclusion (page 24495, lines 13-15) by the sentences:

29 "The GOES-retrieved clouds applied here adjusted only the modeled photolysis rates, while  
30 modeled clouds continued to drive the dynamics and aqueous phase chemistry. This

inconsistency in the placement of clouds is similar to the approach of a previous study (Pour-Biazar et al., 2007). Thus, this work demonstrates a sensitivity study of using satellite-derived photolysis rates on model performance rather than a full integration of satellite-observed clouds into all aspects of the model. Future work could extend the use of GOES-retrieved clouds to also correct model dynamics and aqueous phase chemistry and investigate their impacts on NO<sub>x</sub> and O<sub>3</sub> modeling.”

2. *The last sentence of the introduction states that the manuscript will also present inverse modeling of VOC emissions, but there is no mention of this in the methodology. Some results of VOC inversions are presented in the Conclusions and the reader is directed to supplementary information. If this analysis is to be presented as one of the main aims of the manuscript, I think that the methodology and results should appear earlier in the manuscript.*

The reason we studied VOC is that we want to see if the uncertainties in VOC emissions will significantly affect our NO<sub>x</sub> inversion results. Since this is not the main aim of this paper and the findings are not significant, we have moved the description of VOC emissions part in the introduction section (page 24480, lines 7-20) into the supplementary material. We keep the last sentence regarding the VOC work in the introduction section (page 22481, lines 1-2) and point it directly to the supplement.

3. *The last sentence of the 2.5.1 states that the “the OMI averaging kernels are not applied here.” I think this is misleading because it implies that the vertical sensitivity of the retrieval and dependence on the a-priori profile are ignored. This is in fact not the case, as is shown in the supplement, and I would urge the authors to reword this.*

We have changed the sentence in page 24486, lines 12-14 to “Since applying OMI averaging kernels (Eskes and Boersma, 2003) may introduce more uncertainties to the CAMx-derived NO<sub>2</sub> VCD in this case (Supplement, Sect. 1), the CAMx modeled NO<sub>2</sub> are compared to the OMI NO<sub>2</sub> directly.” to avoid any confusion.

Specific comments:

1. *Page 24478 Line 13: The term ‘ozone design values’ is not common outside of U.S. air quality policy circles. Thus a typical reader may not understand the implications of ozone design values above the NAAQS standard. It might be good here to give a brief definition of the term, or phrase this in a different way.*

We have removed the term “ozone design value” and rephrased the sentence in page 24478, lines 11-17 to “First and foremost, the Houston-Galveston-Brazoria (HGB) region and the Dallas-Fort Worth (DFW) region exceed the 2008 O<sub>3</sub> National Ambient Air Quality Standard (NAAQS) of 75 ppb and thus are both classified by US Environmental Protection Agency (US EPA) as O<sub>3</sub> non-attainment areas. Next, Beaumont-Port Arthur (BPA), Northeast Texas (NE Texas), and Austin and San Antonio regions require attention for closely approaching that standard (Gonzales and Williamson, 2011).”

2. *I think it’s misleading to say that GOES measures cloud fraction. The 12 km cloud fraction is derived from the fraction of GOES subpixels that are deemed cloudy. This should at least be made more clear.*

We agree with reviewer on this point. The cloud fraction in the 12km model grid was integrated from GOES sub-pixels. The terms we use in our paper are “GOES-retrieved clouds” and “GOES-derived photolysis rates”. We have changed the sentence in page 24483, lines 11-12 to “In this study, hourly GOES observations with integrated 12km cloud properties from sub-pixels have been used.” to avoid any confusion.

## References

Eskes, H. J. and Boersma, K. F.: Averaging kernels for DOAS total column satellite retrievals. *Atmos. Chem. Phys.*, 3, 1285–1291, 2003.

- 1 Gonzales, M. and Williamson, W.: Updates on the National Ambient Air Quality Standards and  
2 the State Implementation Plans for Texas, presented in TCEQ Trade Fair, Austin, TX, 4  
3 May, 2011.
- 4 Pour-Biazar, A., McNider, R. T., Roselle, S. J., Suggs, R., Jedlovec, G., Byun, D. W.,  
5 Kim, S., Lin, C. J., Ho, T. C., Haines, S., Dornblaser, B., and Cameron, R.: Correcting  
6 photolysis rates on the basis of satellite observed clouds. *J. Geophys. Res.*, 112, D10302,  
7 doi: 10.1029/2006JD007422, 2007.
- 8

9

10 **List of changes in the revised manuscript:**

11

- 12 1. A sentence “The region-based DKF inversion suggests increasing NO<sub>x</sub> emissions in most  
13 regions, deteriorating the model performance in predicting ground-level NO<sub>2</sub> and O<sub>3</sub>” was  
14 added to the abstract.
- 15 2. References to Martin et al., (2003); Müller and Stavrou, (2005); Jaeglé et al., (2005); Lin et  
16 al., (2010); Konovalov et al., (2006, 2008); Napelenok et al., (2008); Kurokawa et al., (2009);  
17 Zhao and Wang, (2009); Chai et al., (2009); and Zyrichidou et al., (2015) were added to the  
18 Introduction (page 24479, line 15) and Reference sections.
- 19 3. The number of “50%” in Page 24491, line 23 was revised to “49%”.
- 20 4. The sentence in page 24493, lines 15-17 was revised to “The model performance is also  
21 improved compared against P-3 measurements. For NO<sub>2</sub>, NMB is reduced from 0.09 to -0.02,  
22 and NME is reduced by 0.09. For NO<sub>y</sub>, NMB is reduced by 0.16 and NME is reduced by  
23 0.11 (Table 5).”
- 24 5. The sentences “The GOES-retrieved clouds applied here adjusted only the modeled  
25 photolysis rates, while modeled clouds continued to drive the dynamics and aqueous phase  
26 chemistry. This inconsistency in the placement of clouds is similar to the approach of a  
27 previous study (Pour-Biazar et al., 2007). Thus, this work demonstrates a sensitivity study of  
28 using satellite-derived photolysis rates on model performance rather than a full integration of  
29 satellite-observed clouds into all aspects of the model. Future work could extend the use of  
30 GOES-retrieved clouds to also correct model dynamics and aqueous phase chemistry and  
31 investigate their impacts on NO<sub>x</sub> and O<sub>3</sub> modeling.” were added to Conclusion (page 24495,  
32 line 14).



6. The description of VOC emissions part in the introduction section (page 24480, lines 7-20) was moved to the supplement.
7. The sentence in page 24486, lines 12-14 was revised to “Since applying OMI averaging kernels (Eskes and Boersma, 2003) may introduce more uncertainties to the CAMx-derived NO<sub>2</sub> VCD in this case (Supplement, Sect. 1), the CAMx modeled NO<sub>2</sub> are compared to the OMI NO<sub>2</sub> directly.”
8. The sentences in page 24478, lines 11-17 were rephrased to “First and foremost, the Houston-Galveston-Brazoria (HGB) region and the Dallas-Fort Worth (DFW) region exceed the 2008 O<sub>3</sub> National Ambient Air Quality Standard (NAAQS) of 75 ppb and thus are both classified by US Environmental Protection Agency (US EPA) as O<sub>3</sub> non-attainment areas. Next, Beaumont-Port Arthur (BPA), Northeast Texas (NE Texas), and Austin and San Antonio regions require attention for closely approaching that standard (Gonzales and Williamson, 2011).”
9. The sentence in page 24483, lines 11-12 was revised to “In this study, hourly GOES observations with integrated 12km cloud properties from sub-pixels have been used.”

# **Influence of satellite-derived photolysis rates and NO<sub>x</sub> emissions on Texas ozone modeling**

Wei Tang<sup>1,\*</sup>, Daniel S. Cohan<sup>1</sup>, Arastoo Pour-Biazar<sup>2</sup>, Lok N. Lamsal<sup>3,4</sup>, **Andrew T. White<sup>5</sup>**, Xue Xiao<sup>1</sup>, Wei Zhou<sup>1</sup>, Barron H. Henderson<sup>6</sup>, **Benjamin F. Lash<sup>1</sup>**

<sup>1</sup>*Department of Civil and Environmental Engineering, Rice University, 6100 Main Street MS 519, Houston, TX 77005, USA; Email: [cohan@rice.edu](mailto:cohan@rice.edu)*

<sup>2</sup>*Earth System Science Center, University of Alabama, Huntsville, AL, USA*

<sup>3</sup>*NASA Goddard Space Flight Center, Greenbelt, MD, USA*

<sup>4</sup>*Goddard Earth Sciences Technology & Research, Universities Space Research Association, Columbia, MD, USA*

<sup>5</sup>*Department of Atmospheric Science, University of Alabama, Huntsville, AL, USA*

<sup>6</sup>*Department of Environmental Engineering Sciences, University of Florida, Gainesville, FL, USA*

*\*now at: Chinese Research Academy of Environmental Sciences, Beijing, China*

## **Abstract**

Uncertain photolysis rates and emission inventory impair the accuracy of state-level ozone (O<sub>3</sub>) regulatory modeling. Past studies have separately used satellite-observed clouds to correct the model-predicted photolysis rates, or satellite-constrained top-down NO<sub>x</sub> emissions to identify and reduce uncertainties in bottom-up NO<sub>x</sub> emissions. However, the joint application of multiple satellite-derived model inputs to improve O<sub>3</sub> State Implementation Plan (SIP) modeling has rarely been explored. In this study, Geostationary Operational Environmental Satellite (GOES) observations of clouds are applied to derive the photolysis rates, replacing those used in Texas SIP modeling. This changes modeled O<sub>3</sub> concentrations by up to 80ppb and improves O<sub>3</sub> simulations by reducing modeled normalized mean bias (NMB) and normalized mean error (NME) by up to 0.1. A sector-based discrete Kalman filter (DKF) inversion approach is incorporated with the Comprehensive Air Quality Model with extensions (CAMx)-Decoupled

Direct Method (DDM) model to adjust Texas NO<sub>x</sub> emissions using a high resolution Ozone Monitoring Instrument (OMI) NO<sub>2</sub> product. The discrepancy between OMI and CAMx NO<sub>2</sub> vertical column densities (VCDs) is further reduced by increasing modeled NO<sub>x</sub> lifetime and adding an artificial amount of NO<sub>2</sub> in the upper troposphere. The region-based DKF inversion suggests increasing NO<sub>x</sub> emissions by 10-50% in most regions, deteriorating the model performance in predicting ground NO<sub>2</sub> and O<sub>3</sub>, while the sector-based DKF inversion tends to scale down area and non-road NO<sub>x</sub> emissions by 50%, leading to a 2-5ppb decrease in ground O<sub>3</sub> predictions. Model performance in simulating ground NO<sub>2</sub> and O<sub>3</sub> are improved using sector-based inversion constrained NO<sub>x</sub> emissions, with 0.25 and 0.04 reductions in NMBs and 0.13 and 0.04 reductions in NMEs, respectively. Using both GOES-derived photolysis rates and OMI-constrained NO<sub>x</sub> emissions together reduces modeled NMB and NME by 0.05 and increases the model correlation with ground measurement in O<sub>3</sub> simulations and makes O<sub>3</sub> more sensitive to NO<sub>x</sub> emissions in the O<sub>3</sub> non-attainment areas.

## 1. Introduction

Tropospheric O<sub>3</sub> is a secondary air pollutant formed via the reactions between nitrogen oxides (NO<sub>x</sub> = NO + NO<sub>2</sub>) and volatile organic compounds (VOCs) with heat and sunlight (Seinfeld and Pandis, 2006). Eastern Texas is one of the most populous areas in the United States and has been suffering from O<sub>3</sub> pollution for decades due to large anthropogenic emission sources such as motor vehicles, petrochemical facilities, and coal-burning power plants with unique meteorological conditions of extended heat and humidity and intense solar radiation (Kleinman et al., 2002; Ryerson et al., 2003; Daum et al., 2004; Rappenglück et al., 2008; Kim et al., 2011; Zhou et al., 2014).

1           In eastern Texas, several regions require careful air quality planning for O<sub>3</sub> reductions.  
2   First and foremost, the Houston-Galveston-Brazoria (HGB) region and the Dallas-Fort Worth  
3   (DFW) region exceed the 2008 O<sub>3</sub> National Ambient Air Quality Standard (NAAQS) of 75 ppb  
4   and thus are both classified by US Environmental Protection Agency (US EPA) as O<sub>3</sub> non-  
5   attainment areas. Next, Beaumont-Port Arthur (BPA), Northeast Texas (NE Texas), and Austin  
6   and San Antonio regions require attention for closely approaching that standard (Gonzales and  
7   Williamson, 2011).

8           To comply with the O<sub>3</sub> NAAQS, the U.S. EPA requires the Texas Commission on  
9   Environmental Quality (TCEQ) to identify regulatory strategies using photochemical air quality  
10   models for attaining the O<sub>3</sub> standard in non-attainment areas. However, model uncertainties may  
11   impair the accuracy of model performance and potentially misdirect emission control strategies  
12   (Fine et al., 2003; Digar and Cohan, 2010; Simon et al., 2012). Recent studies show that  
13   uncertain bottom-up emission inventories and modeled photolysis rates are two leading  
14   uncertainties in O<sub>3</sub> modeling (Deguilaume et al., 2007; Digar et al., 2011) and can significantly  
15   impact simulated O<sub>3</sub> concentrations and their sensitivities in Texas (Cohan et al., 2010; Xiao et  
16   al., 2010). Hence, identifying and reducing these uncertainties are essential to ensuring the  
17   reliability of regulatory decision making.

18          Direct measurements of emissions and photolysis rates are spatially limited and  
19   impractical to perform covering the entire modeling domain. However, satellite-based  
20   measurements provide a valuable opportunity to observe some atmospheric parameters and air  
21   pollutants from space and generate a rich measurement dataset with great spatial coverage. Pour-  
22   Biazar et al. (2007) used the GOES-based cloud information to reproduce photolysis rates in the

Community Multiscale Air Quality (CMAQ) model. Results showed large differences between model-predicted and satellite-derived photolysis rates, leading to significant changes in modeled  $O_3$  concentrations. Guenther et al. (2012) found that the Weather Research and Forecasting (WRF) and MM5 models, which are usually used to generate meteorological fields for CAMx or CMAQ, underpredict cloud fractions, leading to more modeled solar radiation reaching the ground and overestimations of modeled photolysis rates and sunlight-sensitive biogenic emissions.

Studies using satellite  $NO_2$  measurements to create top-down  $NO_x$  emissions for atmospheric modeling have also shown promising results (Streets et al., 2013; Martin et al., 2003; Müller and Stavrakou, 2005; Jaeglé et al., 2005; Lin et al., 2010; Konovalov et al., 2006, 2008; Napelenok et al., 2008; Kurokawa et al., 2009; Zhao and Wang, 2009; Chai et al., 2009; Zyrichidou et al., 2015). Most recently, Tang et al. (2013) performed region-based DKF inversions using OMI  $NO_2$  data to adjust  $NO_x$  emission inventory used in Texas SIP modeling; however, results showed that the region-based DKF inversions with National Aeronautics and Space Administration (NASA) OMI  $NO_2$  standard product, version 2, tended to scale up the  $NO_x$  emission inventory by factors of 1.02 to 1.84 and deteriorated model performance as evaluated by ground  $NO_2$  and  $O_3$  monitors.

A challenge of using satellite data for inverse modeling is that atmospheric models are primarily evaluated based on ground-level data, and may not accurately simulate pollutants aloft. Several studies (Hudman et al., 2007; Henderson et al., 2011; Allen et al., 2012; ENVIRON, 2013) have demonstrated that models tend to underestimate upper tropospheric  $NO_2$  level even after lightning and aviation  $NO_x$  sources are included. Though the reason is unclear,

underestimation could result from errors in the chemical mechanism in simulating NO<sub>x</sub> sinks (Mollner et al., 2010; Henderson et al., 2012, Lin et al., 2012, Stavrakou et al., 2013). Efforts to eliminate low bias for upper tropospheric NO<sub>2</sub> simulations over Texas have been unsuccessful to date (ENVIRON 2013). Another discrepancy often noted between models and satellite data is a narrower spread between urban and rural NO<sub>2</sub> in satellite observations (Streets et al., 2013). Recently developed high resolution OMI NO<sub>2</sub> retrievals increase the rural-urban spread, which may decrease the difference between models and satellite observations.

In this work, first, GOES-derived photolysis rates are applied to the CAMx model, and the influence on the modeled NO<sub>2</sub> and O<sub>3</sub> is investigated. Second, the model shortcomings of underestimating upper tropospheric and rural NO<sub>2</sub> demonstrated in Tang et al. (2013) are further addressed by comparing with aircraft measurements and reducing the reaction rate constant of the reaction OH + NO<sub>2</sub> to increase modeled NO<sub>x</sub> lifetime. Third, the sector-based DKF inversion using the recently developed NASA high resolution OMI NO<sub>2</sub> product to Texas NO<sub>x</sub> emissions is explored and compared to the region-based DKF inversion. In addition, inverse modeling is extended to adjust Texas VOC emissions via directly comparing modeled VOC concentrations with ground observations (Supplement, Sect. 4).

## **2. Methodology**

### **2.1 CAMx modeling**

CAMx version 5.3 (ENVIRON, 2010) with the Carbon Bond version 2005 (CB-05) chemical mechanism was used to simulate a SIP modeling episode developed by TCEQ for the HGB O<sub>3</sub> attainment demonstration (Fig. 1) from 13 August to 15 September 2006, coinciding with the intensive measurement campaign TexAQS 2006. The meteorology fields were modeled by the

NCAR/Penn State (National Center for Atmospheric Research/Pennsylvania State University) Mesoscale Model, Version 5, release 3.7.3 (MM5v.3.7.3) (Grell et al., 1994), and the boundary conditions were taken from the Model for Ozone and Related Chemical Tracers (MOZART) global model (ENVIRON, 2008). The base case emission inventory for HGB SIP modeling was provided by TCEQ (TCEQ, 2010). Lightning and aviation NO<sub>x</sub> emissions were added into the base emission inventory. The lightning NO<sub>x</sub> emission is developed based on the measured National Lightning Detection Network (NLDN) data with intra-cloud flashes assumed to be three times of cloud-to-ground flashes and 500 moles NO emissions per flash (Kaynak et al., 2008), and the aviation NO<sub>x</sub> emissions, obtained from the Emission Database for Global Atmospheric Research (EDGAR), were placed at the model height of 9km. The soil NO<sub>x</sub> emission was doubled from its base value because the Yienger and Levy method (YL95) (Yienger and Levy, 1995) has been found to underpredict soil NO<sub>x</sub> by around a factor of 2 over the United States (Hudman et al., 2010). More details about the model inputs and configurations, the emission inventory development, and evaluations of model meteorological inputs can be found in Tang et al. (2013).

## **2.2 GOES-derived photolysis rates**

The photolysis rate calculations in CAMx include two steps (ENVIRON, 2010). First, a Tropospheric Ultraviolet and Visible (TUV) Radiation Model developed by the National Center for Atmospheric Research (NCAR) is used to generate a multi-dimensional table of clear sky photolysis rates (Madronich, 1987; NCAR, 2014) as inputs for the CAMx model as shown in Eq. (1).

Clear sky photolysis rates ( $s^{-1}$ ) are calculated as:

$$J = \int_{\lambda_i}^{\lambda_2} \sigma(\lambda) \phi(\lambda) F(\lambda) d\lambda \quad (1)$$

where  $\sigma(\lambda)$  ( $m^2/molecule$ ) is the absorption cross-section,  $\lambda$  is the wavelength ( $\mu m$ ),  $\phi(\lambda)$  is the quantum yield ( $molecules/photon$ ), and  $F(\lambda)$  is the actinic flux ( $photons/m^2/s/\mu m$ ).

Second, the tabular clear sky photolysis rates are interpolated into each grid cell in the modeling domain and adjusted based on cloud information generated by the meteorology model in standard operational procedure, as shown in Eqs. (2) and (3). Below the cloud, photolysis rates are adjusted as (Chang et al., 1987):

$$J_{below} = J_{clear} [1 + f_c (1.6 tr_c \cos(\theta) - 1)] \quad (2)$$

Above the cloud, photolysis rates are modified as:

$$J_{above} = J_{clear} [1 + f_c \cos(\theta)(1 - tr_c)] \quad (3)$$

where  $f_c$  is the cloud fraction for a grid cell,  $tr_c$  is cloud transmissivity at each model grid layer, and  $\theta$  is the solar zenith angle.

In CAMx,  $tr_c$  is calculated using Eq. (4) (Stephens, 1978),

$$tr_c = \frac{5 - e^{-\tau_c}}{4 + 3\tau_c(1 - \beta)} \quad (4)$$

where  $\tau_c$  is the cloud optical depth simulated in the model and  $\beta$  is the scattering phase-function asymmetry factor assumed to be 0.86 (Chang et al., 1987). The  $f_c$  in each grid cell is predicted by the MM5 model.



GOES-observed cloud properties recover  $f_c$  and broadband  $tr_c$ , which can be used directly in Eqs. (2) and (3) to adjust photolysis rates below and above the clouds, bypassing the need for estimating those values in the model. Within the cloud, the photolysis rates are adjusted via the interpolation of calculated values between satellite-retrieved cloud top and model-estimated cloud base. GOES is capable of measuring cloud properties with spatial resolution down to 1-km and temporal resolution down to an hour or less (Haines et al., 2004), ensuring the sufficient spatial and temporal data coverage for the modeling episode. **In this study, hourly GOES observations with integrated 12km cloud properties from sub-pixels have been used.** However, due to the satellite data availability, satellite-retrieved  $f_c$  and broadband  $tr_c$  may not be available in the early morning and late afternoon. In such cases, the  $f_c$  and  $tr_c$  generated by standard operational procedures in CAMx will be used. More details regarding satellite retrievals of  $f_c$  and  $tr_c$  can be found at Pour-Biazar, et al. 2007.

### **2.3 Emission regions and sectors for the inversion**

As in Tang et al. (2013), an inversion region inside the 12km model domain is designed for both region-based and sector-based DKF inversions, including five urban areas HGB, DFW, BPA, NE Texas, and Austin and San Antonio, surrounded by a north rural area (N rural) and a south rural area (S rural) (Fig. 1).

Six separate  $\text{NO}_x$  emission sectors, area, non-road mobile, on-road mobile, biogenic, electric generating units (EGU) and non-EGU point sources are provided by TCEQ. Lightning and aviation  $\text{NO}_x$  emission sectors were developed in Tang et al. (2013) and added into base emission inventory as independent elevated sources (Table 1). Area sources, including small-scale industry and residential sources such as oil and gas production, gas stations and restaurants,

1 contribute 10% of total emissions in the entire inversion region and 25% in NE Texas in the base  
2 inventory. Non-road sources, including construction equipment, locomotives and commercial  
3 marine, contribute 14% overall. Mobile source emissions by on-road vehicles contribute 27% of  
4 total NO<sub>x</sub> emissions and dominate in the cities such as HGB and DFW. The biogenic NO<sub>x</sub> source  
5 is from soil emissions, which contribute 16% of total NO<sub>x</sub> emissions but dominate in remote  
6 regions. Lightning and aviation sources contribute 8% and 6% to the total emission, respectively.  
7 Non-EGU point sources such as refineries, big boilers and flares, contribute 40% of NO<sub>x</sub>  
8 emissions in BPA and 21% in HGB, the two regions with most of the petrochemical industries.  
9 EGU point emissions are from major power plants with the hourly NO<sub>x</sub> emissions measured by  
10 continuous emissions monitoring (CEM) systems, which are considered the most accurate NO<sub>x</sub>  
11 emission source in the bottom-up emission inventory. Thus, in this study, EGU NO<sub>x</sub> emissions  
12 are assumed to be correct and are not adjusted by DKF inversions.

13 NO<sub>2</sub> sensitivities to NO<sub>x</sub> emission in each emission sector used in the following sector-  
14 based DKF inversions are calculated through DDM (Fig. 5). The biogenic, lightning, and non-  
15 EGU point sources have their own spatial patterns that differ from the other emission sectors. For  
16 example, the aviation source shows strong sensitivity centered from the DFW and HGB regions  
17 and slowly spreading elsewhere. The sensitivities from the area, non-road and on-road sources  
18 have similar spatial patterns concentrated in urban areas due to strong anthropogenic activities,  
19 while the on-road source can be distinguished by the strong highway emissions. Previous studies  
20 (Rodgers, 2000; Curci et al., 2010) indicated that the inversion results would be ill-conditioned  
21 to estimate strongly overlapped sources. Therefore, in this study, the area and non-road sources  
22 are grouped as a single sector in the DKF inversions.

## 2.4 DKF Inversion

Two DKF inversion approaches, region-based and sector-based, are applied in this study to create top-down NO<sub>x</sub> emissions for Texas. The procedure of incorporating DKF method into the CAMx-DDM model was described in detail in Tang et al. (2013).

The DKF inversion process (Prinn 2000), driven by the difference between the measured NO<sub>2</sub> ( $C_{NO_2}^{observed}$ ) and the modeled NO<sub>2</sub> ( $C_{NO_2}^{predicted}$ ), seeks the optimal emission perturbation factors ( $\hat{\mathbf{X}}$ ) (a posteriori) by adjusting NO<sub>x</sub> emissions in each designated emission region or sector iteratively until each a priori emission perturbation factor ( $\mathbf{X}^-$ ) converges within a prescribed criterion, 0.01.

$$\hat{\mathbf{x}}_{NO_x} = \mathbf{x}_{NO_x}^- + \mathbf{P}_{NO_x}^- \mathbf{S}^T (\mathbf{S} \mathbf{P}_{NO_x}^- \mathbf{S}^T + \mathbf{R}_{OMI})^{-1} (\mathbf{C}_{NO_2}^{observed} - \mathbf{C}_{NO_2}^{predicted} - \mathbf{S} \mathbf{x}_{NO_x}^-) \quad (5)$$

$\mathbf{S}$  in Eq. (5), calculated via DDM in this study, is the first-order semi-normalized sensitivity matrix of NO<sub>2</sub> concentrations to either region-based or sector-based NO<sub>x</sub> emissions. The uncertainty value in the measurement error covariance matrix ( $\mathbf{R}$ ) for the OMI observed NO<sub>2</sub> is set to 30% (Bucsela et al., 2013) for all diagonal elements. The uncertainties adopted from Hanna et al. (2001) provide the values for each of the diagonal elements in the emission error covariance matrix ( $\mathbf{P}$ ). A value of 100% is assigned to each emission region, and to the area, non-road, aviation, on-road, and biogenic emission sectors, but a value of 50% is assigned to the non-EGU point emission sector. The uncertainty of lightning NO<sub>x</sub> emissions was estimated in recent studies, ranging from 30% (Martin et al., 2007) to 60% (Schumann and Huntrieser, 2007) on a global scale; thus, the uncertainty value in the lightning sector is set to 50% here. The off-

diagonal elements in **P** are set to zero since each emission component is assumed to be independent.

## **2.5 NO<sub>2</sub> observations**

### **2.5.1 Satellite NO<sub>2</sub> observations**

The Dutch-Finnish OMI aboard the NASA Aura satellite measures daily NO<sub>2</sub> at around 13:40 local time (LT) with the highest spatial resolution of 13×24 km<sup>2</sup> at nadir viewpoint (Levelt et al., 2006a, b; Boersma et al., 2007). Tang et al. (2013) used the NASA OMI standard, version 2.1 (Bucsela et al., 2013; Lamsal et al., 2014) NO<sub>2</sub> retrieval with an a priori profile generated from the Global Modeling Initiative (GMI) model to conduct inverse modeling, and reported an overestimation of NO<sub>2</sub> levels in rural areas. More recently, a high resolution OMI NO<sub>2</sub> retrieval was developed based on the NASA standard product, version 2.1, but using an a priori NO<sub>2</sub> profile generated from nested GEOS-Chem simulations (0.5°×0.666°) with a 2005 emission inventory. Because the emission inventory used in GEOS-Chem simulations includes lightning and other elevated sources, it may better represent the upper tropospheric NO<sub>2</sub> in the retrieval; hence, in this study, the high resolution NASA retrieval is chosen for the DKF inversions. In the high resolution NASA product, only the OMI pixels with sizes less than 16×40km<sup>2</sup> (scan position 10-50) in the clear-sky condition (cloud radiance fraction < 0.5) are selected in creating the gridded data at 0.1°×0.1° resolution and then mapped to the 12km CAMx modeling domain. Since applying OMI averaging kernels (Eskes and Boersma, 2003) may introduce more uncertainties to the CAMx-derived NO<sub>2</sub> VCDs in this case (Supplement, Sect. 1), the CAMx modeled NO<sub>2</sub> are compared to the OMI NO<sub>2</sub> directly (Supplement, Sect. 1).

### 2.5.2 Ground and P-3 aircraft NO<sub>2</sub> observations

The CAMx simulated NO<sub>2</sub> is evaluated by both ground and aircraft measurements. The ground-level NO<sub>2</sub> measurements data are taken from the U.S. EPA Air Quality System (AQS) NO<sub>2</sub> ground monitoring network (Fig. 1) (<http://www.epa.gov/ttn/airs/airsaqs/>). The correction factors (Lamsal et al., 2008; Tang et al., 2013) are applied to the ground measured NO<sub>2</sub> before comparing with the modeled results due to the measurement artifacts in the heated molybdenum catalytic converter used by AQS NO<sub>2</sub> monitors.

The NOAA P-3 aircraft measurements (<http://www.esrl.noaa.gov/csd/tropchem/2006TexAQS/>) are available on 31 August, 11 September, 13 September, and 15 September 2006 in our modeling period. The NO<sub>2</sub> was measured by UV photolysis converter-chemiluminescence (Ryerson et al., 2000), and NO<sub>y</sub> was measured by Au converter-chemiluminescence (Ryerson et al., 1999) aboard the P-3 aircraft, from ground to approximately 5km aloft and with a time resolution of 1-second; thus, hourly averaged P-3 NO<sub>2</sub> and NO<sub>y</sub> are calculated to compare with the modeled data at corresponding time and grid cells.

### 2.5.3 NASA DC-8 flight NO<sub>2</sub> observations

The NO<sub>2</sub> measured by NASA DC-8 flights (<http://www-air.larc.nasa.gov/cgi-bin/arcstat>) during the Intercontinental Chemical Transport Experiment-North America (INTEX-NA) field campaign in 2004 (Singh et al., 2006) is used in this study to evaluate the modeled NO<sub>2</sub> vertical profile, especially in the upper troposphere. The DC-8 flight NO<sub>2</sub> measurements were made on a total of 18 days from 1 July to 14 August 2004, spanning from 7:00 to 20:00 CST with 1-second resolution. The NO<sub>2</sub> was measured by the Thermal Dissociation-Laser Induced Fluorescence (TD-LIF) instrument. TD-LIF measurements of NO<sub>2</sub> can be impacted by methyl peroxy nitrate

(CH<sub>3</sub>O<sub>2</sub>NO<sub>2</sub>) and HO<sub>2</sub>NO<sub>2</sub> in a temperature-dependent manner; thus, corrections based on the method of Browne et al., (2011) are applied before comparing with the modeled profile. The modeled NO<sub>2</sub> in grid cells within the 36km domain are used to match the measurement data in space, and then all measurement data at each model layer are averaged over all measurement time to compare with the monthly 12-h (7:00-20:00LT) averaged modeled data at the corresponding layer. Although the measurements took place in 2004 and our modeling period is in 2006, we assume the inter-annual variation is insignificant because the upper tropospheric NO<sub>2</sub> is mainly contributed by natural sources and cross-tropopause transport.

### **3. Results and Discussion**

#### **3.1 Impact of GOES-derived photolysis rates on modeled NO<sub>2</sub> and O<sub>3</sub>**

The GOES-retrieved cloud fractions and broadband transmissivity as described in section 2.2 are used to adjust the photolysis rates in CAMx. To investigate the impact from GOES-derived photolysis rates, the differences of modeled ground-level NO<sub>2</sub> photolysis rate ( $J_{\text{NO}_2}$ ), NO<sub>2</sub>, and O<sub>3</sub> between CAMx modeling with and without the GOES-retrieved cloud fractions and transmissivity are calculated.

Using GOES-observed clouds corrects the cloud underprediction issue in the current meteorological models (Pour-Biazar et al., 2007; Guenther et al., 2012; ENVIRON 2012), making  $J_{\text{NO}_2}$  decreases over most of the domain in this study. While on the average there is a domain-wide reduction in  $J_{\text{NO}_2}$ , the impact on O<sub>3</sub> production is not uniform (Figs. 2 and 3), mostly paired with the NO<sub>x</sub> emission distributions. The general impact of using GOES observations is that where the  $J_{\text{NO}_2}$  decreases, modeled NO<sub>2</sub> increases, and O<sub>3</sub> decreases (Figs. 2 and 3), indicating that slower photochemical activity inhibits O<sub>3</sub> formation and thus consumes

less NO<sub>2</sub>, and vice versa. However, an exception occurs at places close to the Houston Ship Channel, showing that although the J<sub>NO2</sub> decreases, modeled NO<sub>2</sub> still decreases (Fig. 3b) and O<sub>3</sub> slightly increases (Fig. 3c). This is probably caused by the availability of other pathways for consuming NO<sub>x</sub> in the VOC-rich environment, and the inhibition of NO regeneration due to reduction in photochemical activity. The largest discrepancy of 80ppb in modeled O<sub>3</sub> occurs at 13:00 on 2 September 2006 over the DFW region during the modeling period. At that time, GOES-based modeling showed up to 6 times higher J<sub>NO2</sub> (reaching approximately 36s<sup>-1</sup>), and 10ppb lower NO<sub>2</sub> in this region (Fig. 2). However, the differences in modeled J<sub>NO2</sub>, NO<sub>2</sub>, and O<sub>3</sub> are much more moderate on a monthly 8-h (10:00-18:00) averaged basis, reaching only up to 3s<sup>-1</sup> for J<sub>NO2</sub>, 0.6ppb for NO<sub>2</sub>, and 3ppb for O<sub>3</sub>, with largest discrepancies in the HGB region (Fig. 3). For the changes in O<sub>3</sub> sensitivities, approximately 6% less J<sub>NO2</sub> on a domain-wide makes modeled O<sub>3</sub> overall less sensitive to NO<sub>x</sub> emissions (Fig. 3d) and more sensitive to VOC emissions (Fig. 3e).

The modeled daily 8-h (10:00-18:00LT) NO<sub>2</sub> and O<sub>3</sub> using either satellite-derived or base model photolysis rates are evaluated by AQS measured data for the entire modeling period. The positive changes in spatiotemporal correlation (R<sup>2</sup>) and negative changes in NMB and NME indicate that satellite-derived photolysis rates improved model performance (Fig. 4). For O<sub>3</sub> simulations (Fig. 4 right), the difference in R<sup>2</sup> increases 1% on average and reaches up to 7% on 26 August, while the differences in NMBs and NMEs decrease 1% on average and reach up to 10% on 11 September, suggesting the satellite-corrected photolysis rates improve the model performance in simulating ground O<sub>3</sub>. However, NMB and NME for NO<sub>2</sub> simulations (Fig. 4 left) do not improve despite an increase in R<sup>2</sup>, probably because other uncertainties in the model and measurements may have a larger impact on NO<sub>2</sub> performance.

### 3.2 Pseudodata test for the sector-based DKF inversion

A controlled pseudodata test was performed in Tang et al. (2013) to test the applicability of the DKF inversion to adjust the  $\text{NO}_x$  emission in each inversion region with the CAMx-DDM model. This showed that the DKF method adjusted the perturbed  $\text{NO}_x$  emission in each region accurately back to its base case. In this study, a similar controlled pseudodata test is conducted to test the applicability of the sector-based DKF inversion with CAMx-DDM.

The pseudodata test for the sector-based DKF inversion is conducted on 10 modeling days (13 August to 22 August), but the modeling results from the first 3 days are discarded to eliminate the model initialization error. A 7-day (16 August to 22 August) averaged modeled  $\text{NO}_2$  VCDs at 13:00-14:00LT with the base case  $\text{NO}_x$  emission inventory is treated as a pseudo-observation, and the one using perturbed  $\text{NO}_x$  emissions in six emission sectors with known perturbation factors ranging from 0.5 to 2.0 (Fig. 6) is used as a priori case. As described in section 2.3, the area and non-road emission sources are considered as one sector (ARNR), and EGU point source is excluded from the inversion. The emission uncertainties are set to 50% for the non-EGU and lightning sectors and to 100% for the others. The measurement error for the pseudo-observation is set to 30%.

The pseudodata test results (Fig. 6 top) show that the a posteriori modeled  $\text{NO}_2$  closely matches the base case modeled value, indicating the DKF inversion is capable of correcting the perturbed  $\text{NO}_x$  emissions in each emission sector. The sensitivity analysis results (Fig. 6 bottom) illustrate that the inversions are insensitive to both emission and observation error covariance matrices for the pseudo-cases.



### 3.3 A priori NO<sub>2</sub> VCDs

The a priori NO<sub>x</sub> emission inventory used in this study is based on the TCEQ base case emission inventory with added lightning and aviation and doubled soil NO<sub>x</sub> emissions (Tang et al., 2013). The reaction rate constant of the reaction NO<sub>2</sub> + OH in CB05 chemical mechanism is reduced by 25% based on Mollner et al. (2010); this tends to increase NO<sub>x</sub> lifetime and transport to rural regions.

To evaluate the extent to which the addition of lightning and aviation NO<sub>x</sub> closes the gap between observed and modeled NO<sub>2</sub> in the upper troposphere noticed by Napelenok et al. (2008), the modeled NO<sub>2</sub> vertical profile is compared with INTEx-NA DC-8 measured NO<sub>2</sub> profiles from the ground to the free troposphere. The comparison (Fig. 7 left) shows that CAMx with the a priori emission inventory strongly overestimates NO<sub>2</sub> near the ground, reasonably agrees with DC-8 NO<sub>2</sub> measurements from 1km to 5km, slightly overestimates NO<sub>2</sub> from 6km to 9km, and slightly underestimates NO<sub>2</sub> from 10km to 15km. The modeled NO<sub>2</sub> profile is further evaluated by the P-3 measured NO<sub>2</sub> from ground to 5km (Fig. 7 right), showing the same pattern of the overestimated surface NO<sub>2</sub> and good agreement with aircraft observations from 1km-5km. The injection of the aviation NO<sub>x</sub> into a single model layer at altitude 6km to 9km rather than more broadly distributed vertically probably causes the overestimation of modeled NO<sub>2</sub> compared to DC-8 at that altitude (ENVIRON, 2013). A low bias of modeled NO<sub>2</sub>, approximately 40ppt, exists in the upper troposphere, from 10km to 15km altitude, which is the CAMx model top layer. Similar low bias of the modeled NO<sub>2</sub> in the upper troposphere compared to the DC-8 measurement also has been found in Allen et al. (2012). Because the low bias in the upper troposphere may arise from model uncertainties other than those associated with emissions (Henderson et al., 2011; 2012), we follow the adjustment approach of Napelenok et al. (2008)

and add 40ppt NO<sub>2</sub> homogeneously to the top layer (10-15km) of the model results when computing the CAMx NO<sub>2</sub> VCDs.

Although the revised CB05 chemical mechanism and artificially added upper tropospheric NO<sub>2</sub> increase modeled NO<sub>2</sub> VCDs in the inversion region by an average of 13% (Supplement, Sect. 2), CAMx modeled NO<sub>2</sub> VCDs remain an average of  $2 \times 10^{14}$  molecules/cm<sup>2</sup> less than OMI observations in rural regions (Fig. 8c).

### **3.4 Top-down NO<sub>x</sub> emissions constrained by DKF inversions**

The DKF inversions with OMI NO<sub>2</sub> are performed to constrain NO<sub>x</sub> emissions in each designated emission region and emission sector. To ensure sufficient spatial coverage, a monthly averaged OMI NO<sub>2</sub> VCD (13 August to 15 September) is calculated and paired with the corresponding modeled NO<sub>2</sub> VCD at satellite passing time (13:00-14:00LT). The DKF inversions are then conducted with 2116 data points covering every grid cell in the inversion region, and the hourly a priori NO<sub>x</sub> emissions are adjusted iteratively until the inversion process converges.

#### **3.4.1 Region-based DKF inversion**

The region-based DKF inversion is conducted to adjust the NO<sub>x</sub> emissions in each inversion region. The inversion results suggest to moderately adjust the a priori NO<sub>x</sub> emissions in most regions with scaling factors ranging from 0.97 to 1.49 (Table 2) and increases NO<sub>2</sub> VCDs by 8% toward OMI measurement over the inversion region (Fig. 8d). Because this inversion is based on a new OMI-retrieved and an improved a priori NO<sub>2</sub> VCDs, the required adjustments in each inversion region are much lower compared to the results in Tang et al. (2013) with scaling factors ranging from 0.56 to 1.98 and 30% increased NO<sub>2</sub> VCDs.

1           The model performance is then evaluated by the ground and aircraft measurements. The  
2   DKF inversion adjusts DFW NO<sub>x</sub> emissions by only 3%, while it adds 49% to BPA emissions  
3   and less than 15% to other urban regions. The NMB and NME of the a posteriori modeled NO<sub>2</sub>  
4   VCDs decrease in every urban area and are reduced from -0.11 to -0.05 and from 0.17 to 0.16  
5   overall compared to OMI. The spatial correlations between monthly averaged OMI and CAMx  
6   NO<sub>2</sub> VCDs ( $R^2$ ) are improved only in the BPA and Austin and San Antonio areas, but the overall  
7   region-wide performance is improved (Table 3). The modeled NO<sub>2</sub> with a priori NO<sub>x</sub> emissions  
8   overpredicts ground-level NO<sub>2</sub> (Table 4); hence, the increase in NO<sub>x</sub> emissions at most urban  
9   places suggested by the inversion actually deteriorates the ground-level NO<sub>2</sub> simulations in all  
10   urban areas except in the DFW region. The modeled NMB and NME of ground O<sub>3</sub> are reduced  
11   in the HGB and BPA regions, but not in DFW, probably because the increased NO<sub>x</sub> in the first  
12   two regions titrates more ground O<sub>3</sub> at night and inhibits O<sub>3</sub> formation during the day, decreasing  
13   the O<sub>3</sub> concentrations which are already overestimated in the a priori simulation (Table 6). No  
14   improvements of model performance are found in simulating P-3 observed NO<sub>2</sub> and NO<sub>y</sub> using  
15   the inverted NO<sub>x</sub> emissions.

16           Applying a single scaling factor to an entire inversion region may not well capture the  
17   NO<sub>x</sub> spatial distributions (Tang et al., 2013). Since DDM can also track the spatial relationship  
18   between modeled NO<sub>2</sub> concentrations and NO<sub>x</sub> emissions in each emission sector, a sector-based  
19   DKF inversion can potentially serve as an alternative approach to constrain NO<sub>x</sub> emissions in  
20   order to have more heterogeneous adjustments in each inversion region.

### 3.4.2 Sector-based DKF inversion

The sector-based DKF inversion is first conducted on six NO<sub>x</sub> emission sectors: area and nonroad (ARNR), on-road, biogenic, aviation, lightning, and non-EGU points (Case I). The scaling factors generated by the inversion ranges from 0.54 to 4.10, with the largest scale-down in the ARNR sector and the largest scale-up in the aviation sector. The inversion reduces NO<sub>x</sub> emission in the biogenic sector by 30% from the a priori inventory which had doubled soil NO<sub>x</sub> from the base model. The inversion leaves on-road, lightning, and non-EGU points sectors nearly unchanged, applying less than 4% adjustments (Table 2). The NO<sub>2</sub> VCD is increased by only 6% toward OMI measurement over the inversion region in this case. Most of the increase in NO<sub>2</sub> VCDs occurs in rural areas, and some declines occur in urban areas (Fig 8e).

The NO<sub>x</sub> emission in each inversion region is recalculated after applying adjustments to each emission sector, and model performance is evaluated by the ground and aircraft measurements. The scaling factors in each region now are different and closer to 1 than those generated by the region-based inversion, ranging from 0.86 in NE TX to 1.17 in DFW. The modeled NMB and NME in simulating OMI NO<sub>2</sub> are all decreased in five urban areas. Within the inversion region, the overall modeled NMB and NME are reduced from -0.11 to -0.04 and from 0.17 to 0.14, respectively using inverted NO<sub>x</sub> emissions (Table 3). The 50% cut in the ARNR sector helps to improve the model performance in simulating ground-level NO<sub>2</sub> and O<sub>3</sub> which had been overestimated using a priori NO<sub>x</sub> emissions. The inverted NO<sub>x</sub> emissions decrease modeled NMB and NME in all five urban areas and overall decrease NMB by 0.25 and 0.04, and NME by 0.13 and 0.04 in simulating ground-level NO<sub>2</sub> and O<sub>3</sub>, respectively (Table 4 and Table 6). The model performance is also improved compared against P-3 measurements. For NO<sub>2</sub>, NMB is reduced from 0.09 to -0.02, and NME is reduced by 0.09. For NO<sub>y</sub>, NMB is

1 reduced by 0.16 and NME is reduced by 0.11 (Table 5). The scaled-down ground NO<sub>x</sub> emissions  
2 lead to a 2-5 ppb lower modeled 8-h (10:00-18:00LT) ground O<sub>3</sub> and make O<sub>3</sub> formation  
3 chemistry less sensitive to the VOC emissions, with reduction of 1-3ppb sensitivity coefficients  
4 over the inversion region. The O<sub>3</sub> sensitivity to NO<sub>x</sub> emissions also decreases by approximately  
5 1-2ppb over most of the inversion region; however, the O<sub>3</sub> formation chemistry in the urban  
6 cores of the DFW, HGB, and Austin and San Antonio regions shifts toward being more NO<sub>x</sub>-  
7 limited, leading to a 1-3 ppb increase of O<sub>3</sub> sensitivity to NO<sub>x</sub> emissions (Fig. 9).

8 Although the inversion improves the model performance, the sensitivity analysis  
9 (Supplement, Sect. 3) shows that the aviation and ARNR sectors are relatively responsive to the  
10 emission uncertainty values and offset each other (Fig. S2), indicating the DKF inversion may  
11 not be capable of fully distinguishing these two emission sectors. Therefore, the aviation source  
12 is then merged with ARNR and the DKF inversion is re-conducted on five emission sectors: area,  
13 nonroad, and aviation (ARNRAV), on-road, biogenic, lightning, and non-EGU points (Case II).  
14 In case II, the inversion results are more stable and insensitive to the emission uncertainties in  
15 each emission sector (Fig. S2). However, the inversion tends to scale up all three source  
16 categories in the ARNRAV sector together by 50% to compensate for the rural NO<sub>2</sub> gap. The  
17 inversion reduces on-road and biogenic NO<sub>x</sub> emissions by 12% and 16%, respectively. The  
18 adjustments for the lightning and non-EGU points sectors are still less than 4% (Table 2). On the  
19 region basis, the inversion tends to increase NO<sub>x</sub> emissions in all regions with increments  
20 ranging from 1% in the Austin and San Antonio region to 18% in the NE TX region; it thus  
21 increases the modeled NO<sub>2</sub> VCDs by 7% on average. The inversed NO<sub>2</sub> VCD in this case is very  
22 similar to that from the region-based inversion (Fig. 8f). The model performance of simulating  
23 OMI NO<sub>2</sub> VCDs is improved and similar to the results from case I (Table 3). However, unlike

case I, no improvements are found in simulating ground measured NO<sub>2</sub> and O<sub>3</sub> and P-3-measured NO<sub>2</sub> and NO<sub>y</sub> using the inverted NO<sub>x</sub> emissions in case II (Table 4-6). Because the ground NO<sub>x</sub> emissions are increased in this case, the inversion impacts the O<sub>3</sub> simulations in the opposite direction than in case I. The modeled 8-h ground O<sub>3</sub> increases by around 2ppb and becomes more sensitive to both NO<sub>x</sub> and VOC emissions over most of the inversion region; however, the O<sub>3</sub> formation chemistry shifts toward being more VOC-limited in DFW and HGB (Fig. 9).

#### 4. Conclusions

Satellite-derived photolysis rates and NO<sub>x</sub> emissions are both applied to a Texas SIP modeling episode to investigate the capabilities of using satellite data to enhance state-level O<sub>3</sub> regulatory modeling. Results show that the ground-level O<sub>3</sub> simulations are improved with reductions of modeled NMB from 0.42 to 0.37 and modeled NME from 0.50 to 0.45 by using GOES-derived photolysis rates and sector-based DKF (case I) with OMI NO<sub>2</sub> inverted NO<sub>x</sub> emission inventory (Table 6). The GOES-derived photolysis rates and OMI-constrained NO<sub>x</sub> emissions decrease monthly averaged 8-h O<sub>3</sub> concentrations by 2-5ppb over the entire inversion region and turn O<sub>3</sub> formation chemistry toward being less sensitive to NO<sub>x</sub> and VOC emissions over most of inversion areas, while being more NO<sub>x</sub> sensitive in the two O<sub>3</sub> nonattainment areas, DFW and HGB (Fig. 10).

Applying GOES-retrieved cloud coverage and transmissivity reduce the modeled photolysis rates over most of the domain, leading to less photochemical activity and O<sub>3</sub> production and shifting O<sub>3</sub> formation chemistry toward being less sensitive to NO<sub>x</sub> emissions,

except in the DFW region where modeled photolysis rates are increased by the GOES retrieval, leading to impacts in the opposite direction. In comparing with the AQS ground measurements, the GOES-derived photolysis rates improve the ground-level O<sub>3</sub> simulations but not the NO<sub>2</sub> simulations, indicating other model errors may dominate the accuracy of model performance in simulating ground-level NO<sub>2</sub>. The GOES-retrieved clouds applied here adjusted only the modeled photolysis rates, while modeled clouds continued to drive the dynamics and aqueous phase chemistry. This inconsistency in the placement of clouds is similar to the approach of a previous study (Pour-Biazar et al., 2007). Thus, this work demonstrates a sensitivity study of using satellite-derived photolysis rates on model performance rather than a full integration of satellite-observed clouds into all aspects of the model. Future work could extend the use of GOES-retrieved clouds to also correct model dynamics and aqueous phase chemistry and investigate their impacts on NO<sub>x</sub> and O<sub>3</sub> modeling.

The DKF inversion approach has been successfully incorporated with the CAMx-DDM model and was conducted on both region-based and sector-based NO<sub>x</sub> emissions. A controlled pseudodata test conducted on the sector-based DKF inversion confirmed that it accurately captures known perturbations in NO<sub>x</sub> emission sectors. In addition to implementing lightning and aviation NO<sub>x</sub> emissions in the upper troposphere and doubling soil NO<sub>x</sub> emissions from the ground, the NO<sub>x</sub> lifetime is increased by reducing 25% the reaction rate constant of the reaction OH + NO<sub>2</sub>. The upper tropospheric NO<sub>2</sub> underestimation is further eliminated by adding a 40ppt homogenous NO<sub>2</sub> layer in the model top. On the other hand, the high resolution OMI retrieval with a priori profile from the nested GEOS-Chem simulation further enhances NO<sub>2</sub> in urban areas and reduces NO<sub>2</sub> in rural. However, the comparison still shows that the OMI has higher NO<sub>2</sub> VCDs than CAMx in rural areas, by around  $2 \times 10^{14}$  molecules/cm<sup>2</sup>. It is not clear that the

discrepancy between OMI and CAMx in rural areas is caused by uncertainties in NO<sub>x</sub> emission inventory or errors in OMI retrieval and other model uncertainties. The OMI NO<sub>2</sub> retrieval can be further improved by using the finer resolution terrain and albedo data (Russell et al., 2011) and observed vertical profiles from aircraft spiral measurements in the recent DISCOVER-AQ Houston measurement campaign (Crawford et al., 2014). The accuracy of CAMx modeled NO<sub>2</sub> VCDs can benefit from further improving the modeled chemical and transport processes (ENVIRON 2013), such as updating NO<sub>x</sub> recycling process to increase NO<sub>x</sub> lifetime, or adding cross-tropopause transport processes to allow more stratospheric NO<sub>2</sub> penetrate to upper troposphere. This may obtain better spatial distribution of modeled NO<sub>2</sub> rather than adding a homogeneous layer at top to compensate the model deficiency.

The region-based DKF inversion still over scales NO<sub>x</sub> emissions in urban areas to compensate for the rural NO<sub>2</sub> differences because the NO<sub>2</sub> VCDs gap in rural areas is not eliminated, leading to 10-50% increase of NO<sub>x</sub> emissions at most regions and worsening the ground-level O<sub>3</sub> simulations; however, the scaling factors generated in this study are much more moderate than those were found in Tang et al. (2013). The sector-based DKF inversion (case I) takes the aviation source to compensate the NO<sub>2</sub> gap in rural area, probably because its relatively spread-out emission pattern over rural area corresponds with the NO<sub>2</sub> discrepancy distributions, leading to appropriate adjustments in the ground emissions and improving both ground-level NO<sub>2</sub> and O<sub>3</sub> simulations; however, the aviation source is unrealistically adjusted by applying a suggested factor of 4 to its base value, and the adjustments offset the area and nonroad sector with varying emission uncertainties in the sensitivity analysis. Although merging the aviation source into the area and nonroad emission sector makes the inversion (case II) more stable, the large scaling factor for the aviation sector is now shared with area and nonroad emissions,



1 leading to area and nonroad NO<sub>x</sub> emissions being scaled up by 50%. Thus, the model  
2 performance in ground-level NO<sub>2</sub> and O<sub>3</sub> simulations is deteriorated and is even worse than the  
3 results generated from the region-based inversion. The lightning NO<sub>x</sub> emissions seem to be well  
4 estimated and are adjusted little by the inversion. However, it may also indicate that the OMI  
5 retrieved NO<sub>2</sub> is insensitive to the lightning source, most probably due to the NO<sub>x</sub> partitioning  
6 predominantly to NO in the upper troposphere and the clear-sky cloud screening criterion used in  
7 the OMI data processing. The NO<sub>2</sub> discrepancy between OMI and CAMx drives the DKF  
8 inversion and is assumed to be mostly contributed by the uncertainties in the NO<sub>x</sub> emission  
9 inventory. However, findings from this study indicate that if the uncertainty in the a priori NO<sub>x</sub>  
10 emissions is low, errors in the satellite retrieval and model itself cannot be neglected, making the  
11 inversion less capable of reducing the uncertainties in the bottom-up NO<sub>x</sub> emission inventory.

12         The region-based DKF inversion applies a single scaling factor to each inversion region,  
13 and assumes the a priori emission pattern in each inversion region is correct, causing  
14 deterioration of the model performance in this case. While the sector-based DKF inversion  
15 applies a single scaling factor to each emission sector, that leads to more heterogeneous  
16 adjustments in each inversion region and relatively better modeling results than those from the  
17 region-based inversion. However, the sector-based inversion assumes the spatial distribution of  
18 NO<sub>x</sub> emissions in each sector is accurately estimated in the bottom-up NO<sub>x</sub> emission inventory,  
19 which is also a simplification. For example, TCEQ recently developed a single-day aviation  
20 emission inventory using the Advanced Emission Model (AEM3) for the new Rider 8 modeling  
21 domain, which has more accurate flight profile and distributes emissions more broadly in the  
22 vertical direction, leading to the spatial pattern of NO<sub>x</sub> emissions somewhat different than that  
23 obtained from EDGAR (ENVIRON 2013). In addition, the newly developed Berkeley-Dalhousie

1 Soil NO<sub>x</sub> Parameterization (BDSNP) scheme (Hudman et al., 2012) recently was implemented  
2 into the CMAQ model to estimate soil NO<sub>x</sub> emissions, showing large spatial and temporal  
3 differences compared to those estimated by the YL95 scheme over eastern Texas. All these  
4 changes described above in the a priori NO<sub>x</sub> emission inventory may have significant impact on  
5 the sector-based inversion results.

6 The direct scaling inversion (Supplement, Sect. 4) using PAMS measured VOCs  
7 improves the model performance in simulating five chosen VOC species and indicates the TCEQ  
8 VOC emission inventory used in HGB SIP modeling is now much better than the previous  
9 reported emissions with values off by an order of magnitude. However, the inverted VOC  
10 emissions have insignificant impact on the ground-level NO<sub>2</sub> and O<sub>3</sub> simulations, probably  
11 because of the limited spatial coverage of the PAMS measurement sites and most VOC-saturated  
12 conditions in the inversion region. Future work could explore the capabilities of using satellite-  
13 observed formaldehyde data to constrain the Texas isoprene or even other anthropogenic VOC  
14 emissions (Defour et al., 2009; Curci et al., 2010).

15 The statistical results show that although the modeled NMB and NME are reduced,  
16 OMI-constrained NO<sub>x</sub> emissions barely improve the spatiotemporal correlations ( $R^2$ ) with  
17 ground-measured NO<sub>2</sub> and O<sub>3</sub>, indicating that either applying the scaling factors generated at the  
18 OMI passing time is unable to reduce the emission uncertainty at each hour or the current OMI  
19 resolution is insufficient to capture the spatial distributions of the NO<sub>x</sub> emission pattern. The  
20 future launch of NASA Tropospheric Emission: Monitoring of Pollution (TEMPO) geostationary  
21 satellite (Streets et al., 2013) could help address these shortcomings by providing a temporal  
22 resolution down to an hour and a spatial resolution down to 4km×4km measurement.

*Acknowledgements.* Funding for this research was provided by the U.S. NASA Research Opportunities in Space and Earth Sciences (ROSES) grant NNX10AO05G and by the NASA Air Quality Applied Science Team. The authors thank Jim McKay and Ron Thomas at TCEQ for providing emission inputs and insightful discussions about the TCEQ emission inventory, Gary Wilson and Greg Yarwood at ENVIRON for CAMx support, Ron Cohen at UC-Berkeley for the INTEX-NA DC-8 NO<sub>2</sub> measurement, and Tom Ryerson, Carsten Warneke, and Joost de Gouw at NOAA for the P-3 NO<sub>2</sub>, NO<sub>y</sub> and VOC measurements.

## References

- Allen, D. J., Pickering, K. E., Pinder, R. W., Henderson, B. H., Appel, K. W., and Prados, A.: Impact of lightning-NO on eastern United States photochemistry during the summer of 2006 as determined using the CMAQ model. *Atmos. Chem. Phys.*, 12, 1737-1758, 2012.
- Boersma, K. F., Eskes, H. J., Veefkind, J. P., Brinksma, E. J., van der A, R. J., Sneep, M., van der Oord, G. H. J., Levelt, P. F., Stammes, P., Gleason, J. F., and Bucsela, E. J.: Near-real time retrieval of tropospheric NO<sub>2</sub> from OMI. *Atmos. Chem. Phys.*, 112, 2103–2118, 2007.
- Browne, E. C., Perring, A. E., Wooldridge, P. J., Apel, E., Hall, S. R., Huey, L. G., Mao, J., Spencer, K. M., St. Clair, J. M., Weinheimer, A. J., Wisthaler, A., and Cohen, R. C.: Global and regional effects of the photochemistry of CH<sub>3</sub>O<sub>2</sub>NO<sub>2</sub>: Evidence from ARCTAS. *Atmos. Chem. Phys.*, 11, 4209–4219, 2011.
- Bucsela, E. J., Krotkov, N. A., Celarier, E. A., Lamsal, L. N., Swartz, W. H., Bhartia, P. K., Boersma, K. F., Veefkind, J. P., Gleason, J. F., and Pickering, K. E.: A new stratospheric and tropospheric NO<sub>2</sub> retrieval algorithm for nadir-viewing satellite instruments: applications to OMI. *Atmos. Meas. Tech.*, 6, 2607–2626, 2013.
- Chai, T., Carmichael, G. R., Tang, Y., Sandu, A., Heckel, A., Richter, A., and Burrows, J. P.: Regional NO<sub>x</sub> emission inversion through a four-dimensional variational approach using SCIAMACHY tropospheric NO<sub>2</sub> column observations. *Atmos. Environ.*, 43, 5046-5055, 2009.
- Chang, J. S., Brost, R. A., Isaksen, I. S. A., Madronich, S., Middleton, P., Stockwell, W. R., and Walcek, C. J.: A 3-dimensional Eulerian acid deposition model - Physical concepts and formulation. *J. Geophys. Res.*, 92, D12, 14681-14700, 1987.
- Cohan, D. S., Koo, B., and Yarwood, G.: Influence of uncertain reaction rates on ozone sensitivity to emissions in Houston. *Atmos. Environ.*, 44, 3101-3109, 2010.
- Crawford, J., Pickering, K., Kleb, M., and Chen, G.: DISCOVER-AQ: Overall objectives and overview of Houston operations during September 2013, presented in 6<sup>th</sup> AQA meeting, Houston, TX, 16 January, 2014.

Curci, G., Palmer, P. I., Kurosu, T. P., Chance, K., and Visconti, G.: Estimating European volatile organic compound emissions using satellite observations of formaldehyde from the Ozone Monitoring Instrument. *Atmos. Chem. Phys.*, 10, 11501–11517, 2010.

Daum, P. H., Kleinman, L. I., Springston, S. R., Nunnemacker, L. J., Lee, Y-N., Weinstein-Lloyd, J., Zheng, J., and Berkowitz, C. M.: Origin and properties of plumes of high ozone observed during Texas 2000 Air Quality Study (TEXAQS 2000). *Geophys. Res. Lett.*, 109, D17306, doi: 10.1029/2003JD004311, 2004.

Deguillaume, L., Beekmann, M., and Menut, L.: Bayesian Monte Carlo analysis applied to regional-scale inverse emission modeling for reactive trace gases. *J. Geophys. Res.*, 112, D02307, doi:10.1029/2006JD007518, 2007.

Digar, A. and Cohan, D. S.: Efficient characterization of pollutant-emission response under parametric uncertainty. *Environ. Sci. Technol.*, 44, 6724–6730, 2010.

Digar, A., Cohan, D. S., and Bell, M. L.: Uncertainties influencing health-based prioritization of ozone abatement strategies. *Environ. Sci. Technol.*, 45, 7761–7767, 2011.

Dufour, G., Wittrock, F., Camredon, M., Beekmann, M., Richter, A., Aumont, B., and Burrows, J. P.: SCIAMACHY formaldehyde observations: constraint for isoprene emission estimates over Europe? *Atmos. Chem. Phys.*, 9, 1647–1664, 2009.

ENVIRON: Boundary Conditions and Fire Emissions Modeling, Final Report to the Texas Commission on Environmental Quality. ENVIRON International Corporation, Novato, CA, 2008.

ENVIRON: CAMx Users' Guide, version 5.30. ENVIRON International Corporation, Novato, CA, 2010.

ENVIRON: Improved the Biogenic Emission Inventories across the West, Final Report to the Western Governors' Association. ENVIRON International Corporation, Novato, CA, 2012.

ENVIRON. Continuation on Use of Satellite Nitrogen Dioxide (NO<sub>2</sub>) Data. Final Report to the Texas Commission on Environmental Quality. ENVIRON International Corporation, Novato, CA, 2013.

Eskes, H. J. and Boersma, K. F.: Averaging kernels for DOAS total column satellite retrievals. *Atmos. Chem. Phys.*, 3, 1285–1291, 2003.

Fine, J., Vuilleumier, L., Reynolds, S., Roth, P., Brown, N.: Evaluating uncertainties in regional photochemical air quality modeling. *Annu. Rev. Env. Resour.* 28, 59–106, 2003.

Gonzales, M. and Williamson, W.: Updates on the National Ambient Air Quality Standards and the State Implementation Plans for Texas, presented in TCEQ Trade Fair, Austin, TX, 4 May, 2011.

Grell, G. A., Dudhia, J., and Stauffer, D.: A description of the fifth-generation PennState/NCAR mesoscale model (MM5), NCAR Technical Note, NCAR/TN 398+SR, Boulder, Colorado, 1994.

Guenther, A. B., Jiang, X., Heald, C. L., Sakulyanontvittaya, T., Duhl, T., Emmons, L. K., and Wang, X.: The Model of Emission of Gases and Aerosols from Nature version 2.1 (MEGAN2.1): an extended and updated framework for modeling biogenic emissions. *Geosci. Model Dev.*, 5, 1471–1492, 2012.

Haines, S. L., Suggs, R. J., and Jedlovec, G. J.: The Geostationary Operational Environmental Satellite (GOES) product generation system. NASA Tech. Memo., TM-2004-213286. NASA, Huntsville, Alabama, 2004.

Hanna, S. R., Lu, Z., Frey, H. C., Wheeler, N., Vukovich, J., Arumachalam, S., and Fernau, M.:

Uncertainties in predicted ozone concentration due to input uncertainties for the UAM-V photochemical grid model applied to the July 1995 OTAG domain. *Atmos. Environ.*, 35, 891-903, 2001.

Henderson, B. H., Pinder, R. W., Crooks, J., Cohen, R. C., Hutzell, W. T., Sarwar, G., Goliff, W. S., Stockwell, W. R., Fahr, A., Mathur, R., Carlton, A. G., and Vizuete, W.: Evaluation of simulated photochemical partitioning of oxidized nitrogen in the upper troposphere. *Atmos. Chem. Phys.*, 11, 275-291, 2011.

Henderson B. H, Pinder, R. W., Crooks, J., Cohen, R. C., Carlton, A. G., Pye, H. O. T., and Vizuete, W.: Combining Bayesian methods and aircraft observations to constrain the HO + NO<sub>2</sub> reaction rate. *Atmos. Chem. Phys.*, 12, 653–667, 2012.

Hudman, R. C., Jacob, D. J., Turquety, S., Leibensperger, E. M., Murray, L. T., Wu, S., Gilliland, A. B., Avery, M., Bertram, T. H., Brune, W., Cohen, R. C., Dibb, J. E., Flocke, F. M., Fried, A., Holloway, J., Neuman, J. A., Orville, R., Perring, A., Ren, X., Sachse, G. W., Singh, H. B., Swanson, A., Wooldridge, P. J.: Surface and lightning sources of nitrogen oxides over the United States: Magnitudes, chemical evolution, and outflow. *J. Geophys. Res.*, 112, D12S05, doi:10.1029/2006JD007912, 2007.

Hudman, R. C., Russell, A. R., Valin, L. C., and Cohen, R. C.: Interannual variability in soil nitric oxide emissions over the United States as viewed from space. *Atmos. Chem. Phys.*, 10, 9943–9952, 2010.

Hudman, R. C., Moore, N. E., Mebust, A. K., Martin, R. V., Russell, A. R., Valin, L. C., and Cohen, R. C.: Steps towards a mechanistic model of global soil nitric oxide emissions: implementation and space based-constraints. *Atmos. Chem. Phys.*, 12, 7779–7795, 2012.

Jaeglé, L., Steinberger, L., Martin, R. V., and Chance, K.: Global partitioning of NO<sub>x</sub> sources using satellite observations: Relative roles of fossil fuel combustion, biomass burning and soil emissions. *Faraday Discuss.*, 130, 407-423, 2005.

Kaynak, B., Hu, Y., Martin, R. V., Russell, A. G., Choi, Y., and Wang, Y.: The effect of lightning NO<sub>x</sub> production on surface ozone in the continental United States. *Atmos. Chem. Phys.*, 8, 5151–5159, 2008.

Kim, S. W., McKeen, S. A., Frost, G. J., Lee, S.-H., Trainer, M., Richter, A., Angevine, W.M., Atlas, E., Bianco, L., Boersma, K. F., Brioude, J., Burrows, J. P., de Gouw, J., Fried, A., Gleason, J., Hilboll, A., Mellqvist, J., Peischl, J., Richter, D., Rivera, C., Ryerson, T., te Lintel Hekkert, S., Walega, J., Warneke, C., Weibring, P., and Williams, E.: Evaluations of NO<sub>x</sub> and highly reactive VOC emission inventories in Texas and their implications for ozone plume simulations during the Texas Air Quality Study 2006. *Atmos. Chem. Phys.*, 11, 11361-11386, 2011.

Kleinman, L. I., Daum, P. H., Imre, D., Lee, Y-N., Nunnemacker, L. J., and Springston, S.R.: Ozone production rate and hydrocarbon reactivity in five urban areas: A case of high ozone concentration in Houston. *Geophys. Res. Lett.*, 29, 1467 10.1029/2001GL014569, 2002.

Konovalev, I. B., Beekmann, M., Richter, A., and Burrows, J. P.: Inverse modeling of the spatial distribution of NO<sub>x</sub> emissions on a continental scale using satellite data. *Atmos. Chem. Phys.*, 6, 1747–1770, 2006.

Konovalev, I. B., Beekmann, M., Burrows, J. P., and Richter, A.: Satellite measurement based estimates of decadal changes in European nitrogen oxides emissions. *Atmos. Chem. Phys.*, 8, 2623–2641, 2008.

Kurokawa, J., Yumimoto, K., Uno, I., and Ohara, T.: Adjoint inverse modeling of NO<sub>x</sub>

emissions over eastern China using satellite observations of NO<sub>2</sub> vertical column densities. Atmos. Environ., 43(11), 1878-1887, 2009.

Lamsal, L. N., Martin, R. V., van Donkelaar, A., Steinbacher, M., Celarier, E. A., Bucsela, E., Dunlea, E. J., and Pinto, J. P.: Ground level nitrogen dioxide concentrations inferred from the satellite borne Ozone Monitoring Instrument. J. Geophys. Res., 113, D16308, doi:10.1029/2007JD009235, 2008.

Lamsal, L. N., Krotkov, N. A., Celarier, E. A., Swartz, W. H., Pickering, K. E., Bucsela, E. J., Martin, R. V., Philip, S., Irie, H., Cede, A., Herman, J., Weinheimer, A., Szykman, J. J., and Knepp, T. N.: Evaluation of OMI operational standard NO<sub>2</sub> column retrievals using in situ and surface-based NO<sub>2</sub> observations. Atmos. Chem. Phys. Discuss., 14, 14519–14573, 2014.

Levelt, P. F., Hilsenrath, E., Leppelmeier, G. W., van den Oord, G. H. J., Bhartia, P. K., Tamminen, J., de Haan, J. F., and Veeckind, J. P.: Science objective of the Ozone Monitoring Instrument. IEEE. T. Geosci. Remote., 44, 1199–1208, 2006.

Levelt, P. F., van den Oord, G. H. J., Dobber, M. R., Malkki, A., Visser, H., de Vries, J., Stammes, P., Lundell, J. O. V., and Saari, H.: The Ozone Monitoring Instrument. IEEE. T. Geosci. Remote., 44, 1093–1101, 2006.

Lin, J. T., McElroy, M. B., and Boersma, K. F.: Constraint of anthropogenic NO<sub>x</sub> emissions in China from different sectors: a new methodology using multiple satellite retrievals. Atmos. Chem. Phys., 9(5), 19205-19241, 2010.

Lin, J. T., Liu, Z., Zhang, Q., Liu, H., Mao, J., and Zhuang, G.: Modeling uncertainties for tropospheric nitrogen dioxide columns affecting satellite-based inverse modeling of nitrogen oxides emissions. Atmos. Chem. Phys., 12, 12255-12275, 2012.

Madronich, S.: Photodissociation in the atmosphere 1. Actinic flux and the effects of ground reflections and clouds. J. Geophys. Res., 92, D8, 9740-9752, doi: 10.1029/JD092iD08p09740, 1987.

Martin, R. V., Jacob, D. J., Chance, K., Kurosu, T. P., Palmer, P. I., and Evans, M. J.: Global inventory of nitrogen oxide emissions constrained by space-based observations of NO<sub>2</sub> columns. J. Geophys. Res., 108(D17), 4537, doi:10.1029/2003JD003453, 2003.

Martin, R. V., Sauvage, B., Folkins, I., Sioris, C. E., Boone, C., Bernath, P., and Ziemke, J.: Space-based constraints on the production of nitric oxide by lightning. J. Geophys. Res., 112, D09309, doi: 10.1029/2006JD007831, 2007.

Mollner, A. K., Valluvadasan, S., Feng, L., Sprague, M. K., Okumura, M., Milligan, D. B., Bloss, W. J., Sander, S. P., Martien, P. T., Harley, R. A., McCoy, A. B., and Carter, W. P. L.: Rate of gas phase association of hydroxyl radical and nitrogen dioxide. Science, 330, 646-649, doi:10.1126/science.1193030, 2010.

Müller, J. F. and Stavrou, T.: Inversion of CO and NO<sub>x</sub> emissions using the adjoint of the IMAGES model. Atmos. Chem. Phys., 5, 1157-1186, 2005.

Napelenok, S. L., Pinder, R. W., Gilliland, A. B., and Martin, R. V.: A method for evaluating spatially-resolved NO<sub>x</sub> emissions using Kalman filter inversion, direct sensitivities, and space-based NO<sub>2</sub> observations. Atmos. Chem. Phys., 8, 5603-5614, 2008.

NCAR. 2011. The Tropospheric Visible and Ultraviolet (TUV) Radiation Model web page. National Center for Atmospheric Research, Atmospheric Chemistry Division, Boulder, Colorado, <http://cprm.acd.ucar.edu/Models/TUV/index.shtml>, last access: September 2014.

Pour-Biazar, A., McNider, R. T., Roselle, S. J., Suggs, R., Jedlovec, G., Byun, D. W., Kim, S.,

- 1 Lin, C. J., Ho, T. C., Haines, S., Dornblaser, B., and Cameron, R.: Correcting photolysis  
2 rates on the basis of satellite observed clouds. *J. Geophys. Res.*, 112, D10302,  
3 doi: 10.1029/2006JD007422, 2007.
- 4 Prinn, R. G.: Measurement equation for trace chemicals in fluids and solution of its inverse, in  
5 *Inverse Methods in Global Biogeochemical Cycles*, vol. 114, edited by Kasibhatla, P.,  
6 Heimann, M., Rayner, P., Mahowald, N., Prinn, R. G., and Hartley, D. E., pp. 3-18, AGU,  
7 Washington, D.C., 2000.
- 8 Rappenglück, B., Perna, R., Zhong, S., and Morris, G.A.: An analysis of the vertical structure of  
9 the atmosphere and the upper-level meteorology and their impact on surface ozone levels  
10 in Houston, Texas. *J. Geophys. Res.*, 113, D17315, doi: 10.1029/2007JD009745, 2008.
- 11 Ryerson, T. B., Trainer, M., Angevine, W. M., Brock, C. A., Dissly, R. W., Fehsenfeld, F. C.,  
12 Frost, G. J., Goldan, P. D., Holloway, J. S., Hubler, G., Jakoubek, R. O., Kuster, W. C.,  
13 Neuman, J. A., Nicks Jr., D. K., Parrish, D. D., Roberts, J. M., and Sueper, D. T.: Effect of  
14 petrochemical industrial emissions of reactive alkenes and NO<sub>x</sub> on tropospheric ozone  
15 formation in Houston, Texas. *J. Geophys. Res.*, 108 D084249, doi:10.1029/2002JD003070,  
16 2003.
- 17 Rodgers, C. D.: *Inverse methods for atmospheric sounding theory and practice*, 1st ed., World  
18 Scientific, Singapore, 2000.
- 19 Russell, A. R., Perring, A. E., Valin, L. C., Hudman, R. C., Browne, E. C., Min, K-E.,  
20 Wooldridge, P. J., and Cohen, R. C.: A high spatial resolution retrieval of NO<sub>2</sub> column  
21 densities from OMI: method and evaluation, *Atmos. Chem. Phys.*, 11, 8543-8554, 2011.
- 22 Ryerson, T. B., Huey, L. G., Knapp, K., Neuman, J. A., Parrish, D. D., Sueper, D. T., and  
23 Fehsenfeld, F. C.: Design and initial characterization of an inlet for gas-phase NO<sub>y</sub>  
24 measurements from aircraft. *J. Geophys. Res.*, 104, 5483–5492, doi:10.1029/1998JD100087,  
25 1999.
- 26 Ryerson, T. B., Williams, E. J., and Fehsenfeld, F. C.: An efficient photolysis system for fast-  
27 response NO<sub>2</sub> measurements. *J. Geophys. Res.*, 105, 26, 447–461,  
28 doi:10.1029/2000JD900389, 2000.
- 29 Schumann, U. and Huntrieser, H.: The global lightning-induced nitrogen oxides source.  
30 *Atmos. Chem. Phys.*, 7, 3823-3907, 2007.
- 31 Seinfeld, J. H. and Pandis, S. N.: *Atmospheric chemistry and physics*. John Wiley & Sons, INC.  
32 New Jersey, 2006.
- 33 Simon, H., Baker, K. R., and Phillips, S.: Compilation and interpretation of photochemical model  
34 performance statistics published between 2006 and 2012. *Atmos. Environ.*, 61, 124–139,  
35 2012.
- 36 Singh, H. B., Brune, W. H., Crawford, J. H., Jacob, D. J., and Russell, P. B.: Overview of the  
37 summer 2004 intercontinental chemical transport experiment – North America (INTEX-A).  
38 *J. Geophys. Res.*, 111, D24S01, doi:10.1029/2006JD007905, 2006.
- 39 Stavrou, T., Müller, J.-F., Boersma, K. F., van der A, R. J., Kurokawa, J., Ohara, T., and  
40 Zhang, Q.: Key chemical NO<sub>x</sub> sink uncertainties and how they influence top-down  
41 emissions of nitrogen oxides. *Atmos. Chem. Phys.*, 13, 9057–9082, 2013.
- 42 Stephens, G. L.: Radiation profiles in extended water clouds. II: Parameterization schemes.  
43 *J. Atmos. Sci.*, 35(11), 2123–2132, 1978.
- 44 Streets, D. G., Canty, T., Carmichael, G. R., de Foy, B., Dickerson, R. R., Duncan, B. N.,  
45 Edwards, D. P., Haynes, J. A., Henze, D. K., Houyoux, M. R., Jacob, D. J., Krotkov, N. A.,

- 1 Lamsal, L. N., Liu, Y., Lu, Z-F., Martin, R. V., Pfister, G. G., Pinder, R. W., Salawitch, R. J.,  
2 and Wecht, K. J.: Emissions estimation from satellite retrievals: A review of current  
3 capability. *Atmos. Environ.*, 77, 1011–1042, 2013.
- 4 Tang, W., Cohan, D. S., Lamsal, L.N., Xiao, X., and Zhou, W.: Inverse modeling of Texas NO<sub>x</sub>  
5 emissions using space-based and ground-based NO<sub>2</sub> observations. *Atmos. Chem. Phys.*, 13,  
6 11005-11018, 2013.
- 7 TCEQ.: Houston-Galveston-Brazoria Attainment Demonstration SIP Revision for the 1997  
8 Eight-Hour Ozone Standard, Austin, TX, 2010.
- 9 TCEQ.: Dallas-Fort Worth Attainment Demonstration SIP Revision for the 1997 Eight-hour  
10 Ozone Standard Non-attainment Area, Austin, TX, 2011.
- 11 Xiao, X., Cohan, D. S., Byun, D. W., and Ngan, F.: Highly nonlinear ozone formation in the  
12 Houston region and implications for emission controls. *J. Geophys. Res.*, 115, D23309,  
13 doi:10.1029/2010JD014435, 2010.
- 14 Yienger, J. J. and Levy, H.: Empirical-model of global soil-biogenic NO<sub>x</sub> emissions. *J. Geophys.*  
15 *Res.*, 100(D6), 11447-11464. doi: 10.1029/95JD00370, 1995.
- 16 Zhao, C. and Wang, Y.: Assimilated inversion of NO<sub>x</sub> emissions over east Asia using OMI NO<sub>2</sub>  
17 column measurements. *Geophys. Res. Lett.*, 36, L06805, doi:10.1029/2008GL037123, 2009.
- 18 Zhou, W., Cohan, D. S., and Henderson, B. H.: Slower ozone production in Houston, Texas,  
19 following emission reductions: evidence from Texas Air Quality Studies in 2000 and 2006.  
20 *Atmos. Chem. Phys.*, 12, 2777-2788, 2014.
- 21 Zyrichidou, I., Koukouli, M. E., Balis, D., Markakis, K., Poupkou, A., Katragkou, E.,  
22 Kioutsioukis, I., Melas, D., Boersma, K. F., van Roozendaal, M.: Identification of surface  
23 NO<sub>x</sub> emission sources on a regional scale using OMI NO<sub>2</sub>. *Atmos. Environ.*, 101, 82-93,  
24 2015.



1 Table 1. NO<sub>x</sub> emission rates for seven sectors in seven inversion regions (tons/day).

Source Region	Area	On-road	Non-road	Biogenic	Aviation	Lightning	Non-EGU points	EGU	Total
HGB	28 (6%)	159 (36%)	71 (16%)	10 (2%)	28 (6%)	21 (5%)	92 (21%)	29 (7%)	438
DFW	35 (8%)	152 (37%)	77 (19%)	60 (14%)	44 (11%)	23 (6%)	19 (5%)	6 (1%)	416
BPA	8 (8%)	24 (24%)	7 (7%)	2 (2%)	3 (3%)	8 (8%)	40 (40%)	8 (8%)	101
NE Texas	43 (25%)	34 (20%)	28 (16%)	2 (1%)	3 (2%)	14 (8%)	9 (5%)	41 (24%)	174
Austin and San Antonio	9 (3%)	113 (37%)	37 (12%)	72 (24%)	12 (4%)	5 (2%)	21 (7%)	34 (11%)	303
N Rural	82 (11%)	161 (21%)	103 (13%)	142 (19%)	51 (7%)	94 (12%)	39 (5%)	91 (12%)	763
S Rural	85 (13%)	123 (18%)	79 (12%)	176 (26%)	30 (4%)	61 (9%)	61 (9%)	57 (8%)	672
Total	290 (10%)	766 (27%)	402 (14%)	464 (16%)	171 (6%)	226 (8%)	281 (10%)	266 (9%)	2866

2 Note: percentage indicates the apportionment of each emission sector to the regional total.

3  
4 Table 2. Scaling factors of region-based and sector-based inversions.

Region-based inversion		Sector-based inversion I		Sector-based inversion II	
Emission region	Scaling factor (unitless)	Emission sector	Scaling factor (unitless)	Emission sector	Scaling factor (unitless)
HGB	1.11	Area	0.54	Area	1.49
DFW	0.97	Non-road	0.54	Non-road	1.49
BPA	1.49	On-road	1.03	On-road	0.88
NE Texas	1.10	Biogenic	0.71	Biogenic	0.84
Austin and San Antonio	1.15	Aviation	4.10	Aviation	1.49
N rural	1.24	Lightning	0.98	Lightning	1.03
S rural	0.98	Non-EGU points	0.96	Non-EGU points	0.96

1 Table 3. Evaluation of CAMx modeled NO<sub>2</sub> using OMI NO<sub>2</sub>.

Inversion region	Priori			Posteriori: region-based inversion			Posteriori: sector-based inversion I			Posteriori: sector-based inversion II		
	R <sup>2</sup>	NMB <sup>b</sup>	NME <sup>c</sup>	R <sup>2</sup>	NMB	NME	R <sup>2</sup>	NMB	NME	R <sup>2</sup>	NMB	NME
HGB	0.57	-0.25	0.36	0.57	-0.17	0.35	0.57	-0.21	0.32	0.57	-0.18	0.34
DFW	0.74	-0.21	0.29	0.72	-0.21	0.28	0.70	-0.12	0.25	0.75	-0.13	0.30
BPA	0.40	-0.46	0.47	0.45	-0.33	0.43	0.37	-0.42	0.43	0.39	-0.43	0.44
NE Texas	0.24	-0.40	0.44	0.24	-0.36	0.43	0.21	-0.39	0.43	0.25	-0.31	0.42
Austin and San Antonio	0.45	-0.25	0.35	0.47	-0.18	0.35	0.43	-0.23	0.33	0.44	-0.23	0.34
Overall <sup>a</sup>	0.74	-0.11	0.17	0.75	-0.05	0.16	0.75	-0.04	0.14	0.75	-0.04	0.16

2 a. Compared to OMI observations in all inversion regions

3 b. Normalized mean bias:  $\Sigma(\text{Mod-Obs})/\Sigma(\text{Obs})$

4 c. Normalized mean error:  $\Sigma|(\text{Mod-Obs})|/\Sigma|(\text{Obs})|$

6 Table 4. Evaluation of CAMx modeled NO<sub>2</sub> using hourly AQS ground-measured NO<sub>2</sub>.

Inversion region	Priori			Posteriori: region-based inversion			Posteriori: sector-based inversion I			Posteriori: sector-based inversion II		
	R <sup>2</sup>	NMB	NME	R <sup>2</sup>	NMB	NME	R <sup>2</sup>	NMB	NME	R <sup>2</sup>	NMB	NME
HGB	0.51	0.46	0.67	0.51	0.61	0.77	0.50	0.26	0.56	0.51	0.59	0.76
DFW	0.49	0.43	0.66	0.49	0.40	0.65	0.48	0.14	0.53	0.50	0.55	0.74
BPA	0.45	0.92	1.02	0.45	1.74	1.77	0.45	0.72	0.86	0.45	0.99	1.08
NE Texas	0.70	0.86	0.93	0.70	1.07	1.12	0.70	0.33	0.52	0.70	1.36	1.40
Austin and San Antonio	0.46	0.60	0.87	0.47	0.80	1.01	0.48	0.37	0.73	0.47	0.58	0.86
Overall <sup>a</sup>	0.51	0.51	0.72	0.48	0.67	0.85	0.50	0.26	0.59	0.51	0.63	0.81

7 a. Compared to all ground sites

1 Table 5. Evaluation of CAMx modeled NO<sub>2</sub> using P-3 aircraft-measured NO<sub>2</sub> and NO<sub>y</sub>.

Statistical parameters	NO <sub>2</sub> <sup>a</sup>				NO <sub>y</sub> <sup>a</sup>			
	Priori	Posteriori: region-based inversion	Posteriori: sector-based inversion I	Posteriori: sector-based inversion II	Priori	Posteriori: region-based inversion	Posteriori: sector-based inversion I	Posteriori: sector-based inversion II
R <sup>2</sup>	0.22	0.23	0.24	0.21	0.34	0.35	0.35	0.34
NMB	0.09	0.15	-0.02	0.17	0.70	0.76	0.54	0.79
NME	0.99	1.03	0.90	1.06	0.98	1.03	0.87	1.04

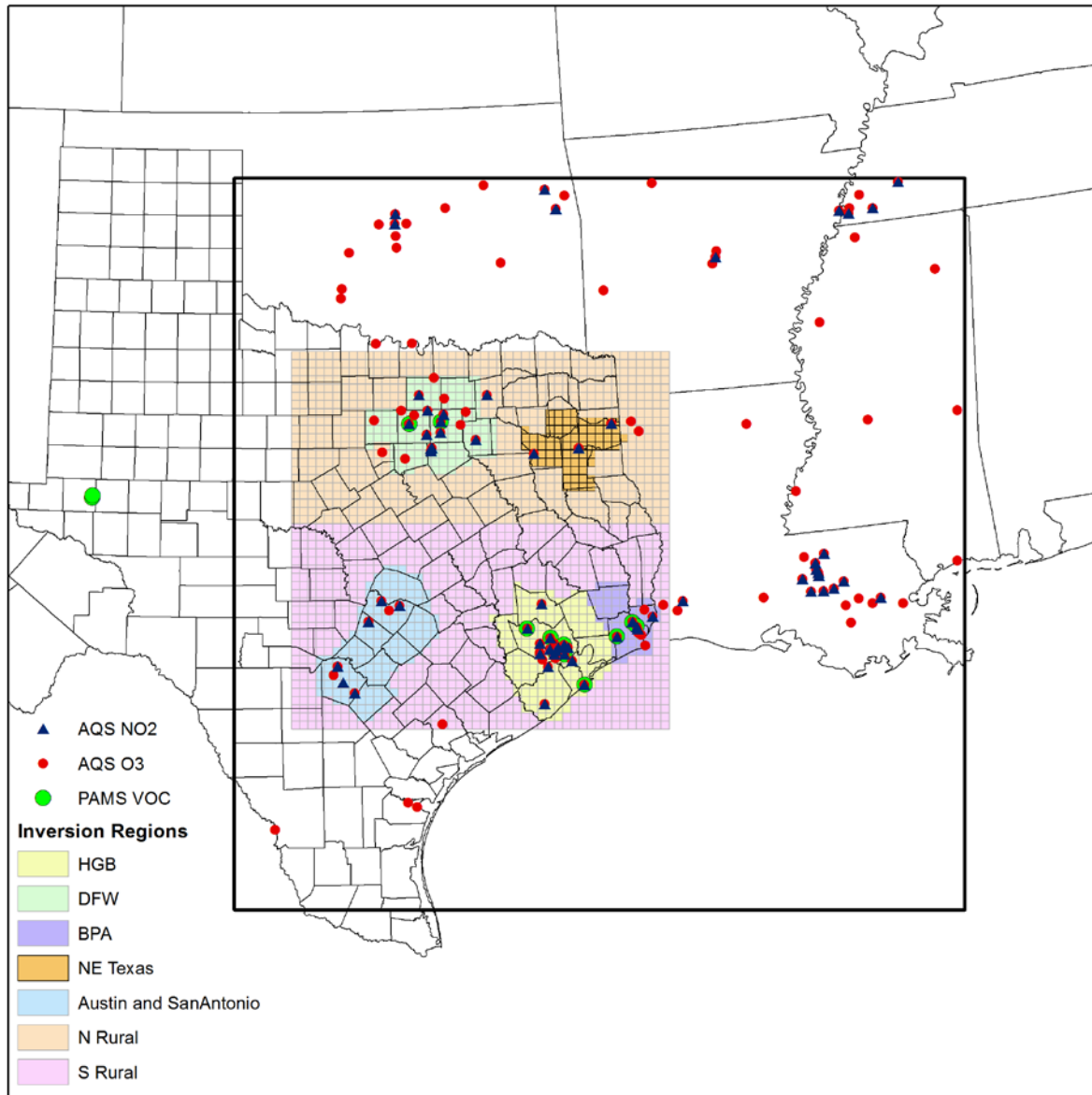
2 a. Comparison available for only four days (August 31, September 11, September 13, and September 15, 2006).

3  
4 Table 6. Evaluation of CAMx modeled O<sub>3</sub> using hourly AQS ground-measured O<sub>3</sub>.

Source region	Priori			Posteriori: region-based inversion			Posteriori: sector-based inversion I			Posteriori: sector-based inversion II			Sector-I inversed NO <sub>x</sub> emissions & GOES photolysis		
	R <sup>2</sup>	NMB	NME	R <sup>2</sup>	NMB	NME	R <sup>2</sup>	NMB	NME	R <sup>2</sup>	NMB	NME	R <sup>2</sup>	NMB	NME
HGB	0.46	0.68	0.75	0.47	0.67	0.74	0.46	0.65	0.72	0.45	0.70	0.76	0.54	0.62	0.69
DFW	0.64	0.21	0.32	0.64	0.23	0.33	0.64	0.18	0.29	0.64	0.21	0.33	0.66	0.18	0.28
BPA	0.47	0.66	0.70	0.47	0.59	0.66	0.49	0.60	0.64	0.45	0.69	0.73	0.52	0.59	0.63
NE Texas	0.49	0.36	0.43	0.49	0.38	0.44	0.50	0.32	0.40	0.48	0.37	0.45	0.55	0.30	0.38
Austin and San Antonio	0.52	0.40	0.46	0.52	0.40	0.46	0.52	0.35	0.43	0.52	0.42	0.48	0.57	0.34	0.41
Overall <sup>a</sup>	0.50	0.42	0.50	0.51	0.42	0.50	0.50	0.38	0.46	0.49	0.43	0.51	0.55	0.37	0.45

5 a. Compared to all ground sites

1



2

3 Figure 1. Seven designated inversion regions in eastern Texas (shaded) within 12-km CAMx  
 4 modeling domain (black square) covered by ground NO<sub>2</sub> monitoring sites (blue triangles), VOC  
 5 monitoring sites (green circles), and O<sub>3</sub> monitoring sites (red circles).

6

7

8

9

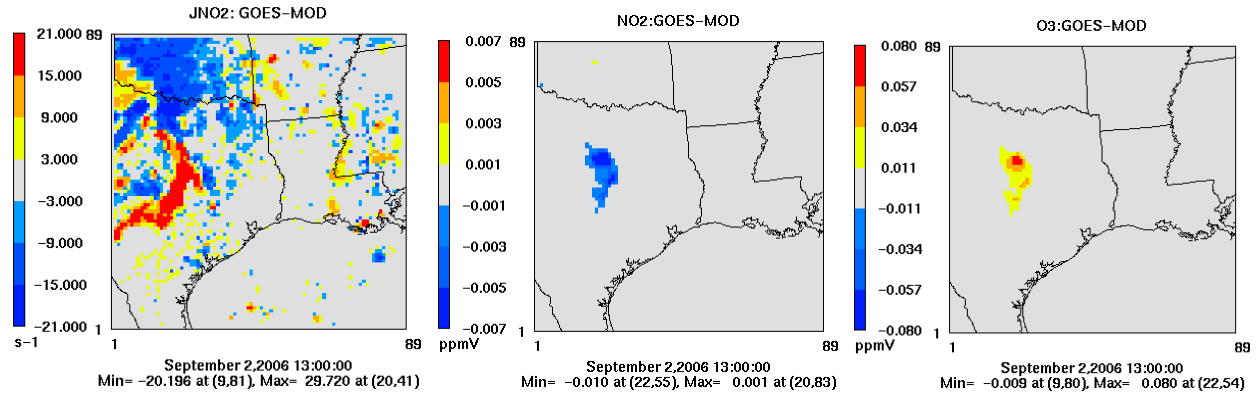


Figure 2. Differences between satellite-derived (GOES) and model predicted (MOD)  $J_{NO_2}$  (left) in simulating  $NO_2$  (middle) and  $O_3$  (right) at 13:00 on 2 September 2006.

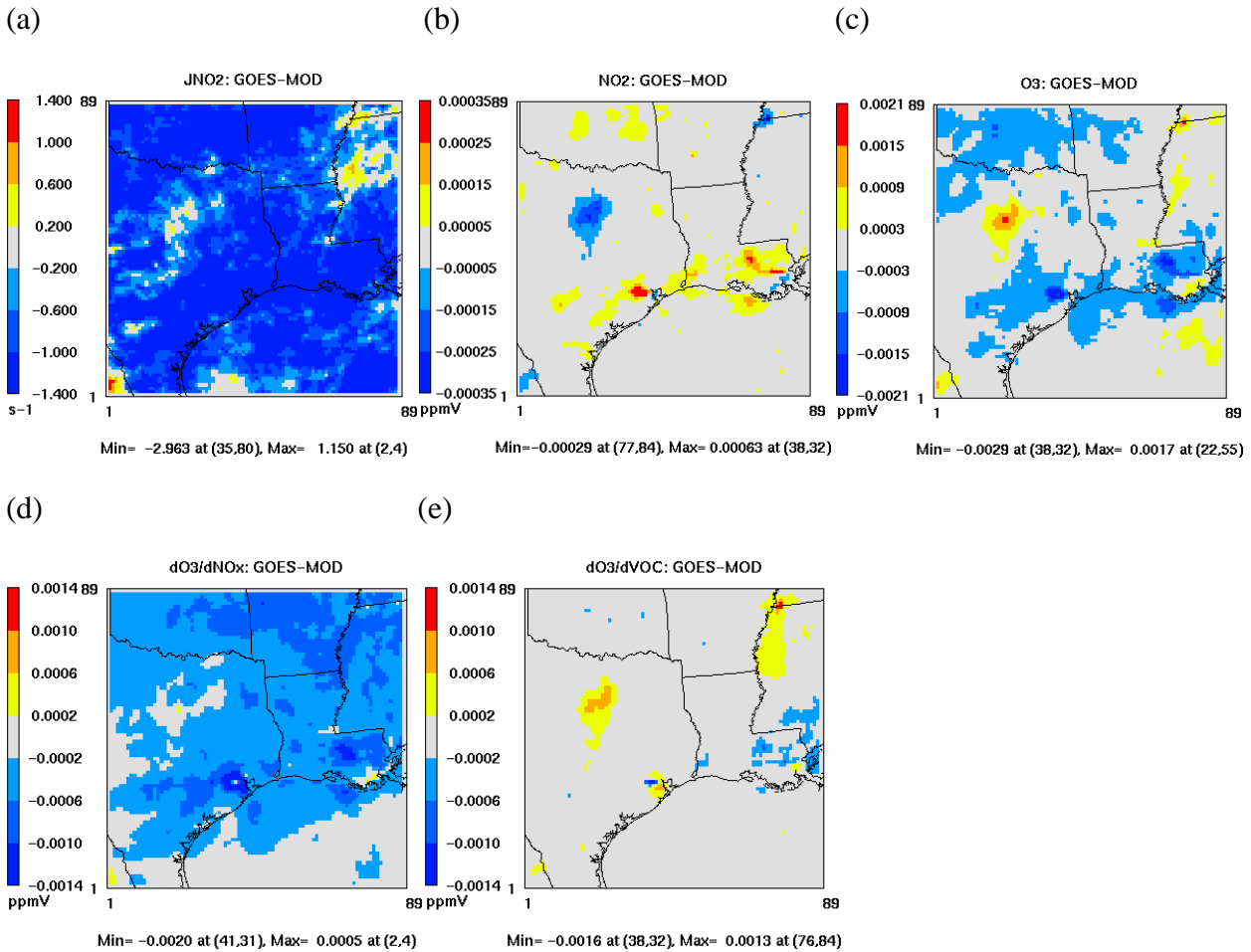


Figure 3. Monthly 8-h (10:00-18:00LT) averaged differences between satellite-derived (GOES) and model predicted (MOD) (a)  $J_{NO_2}$  in simulating (b)  $NO_2$ , (c)  $O_3$ , and  $O_3$  sensitivities to (d)  $NO_x$  and (e) VOC.

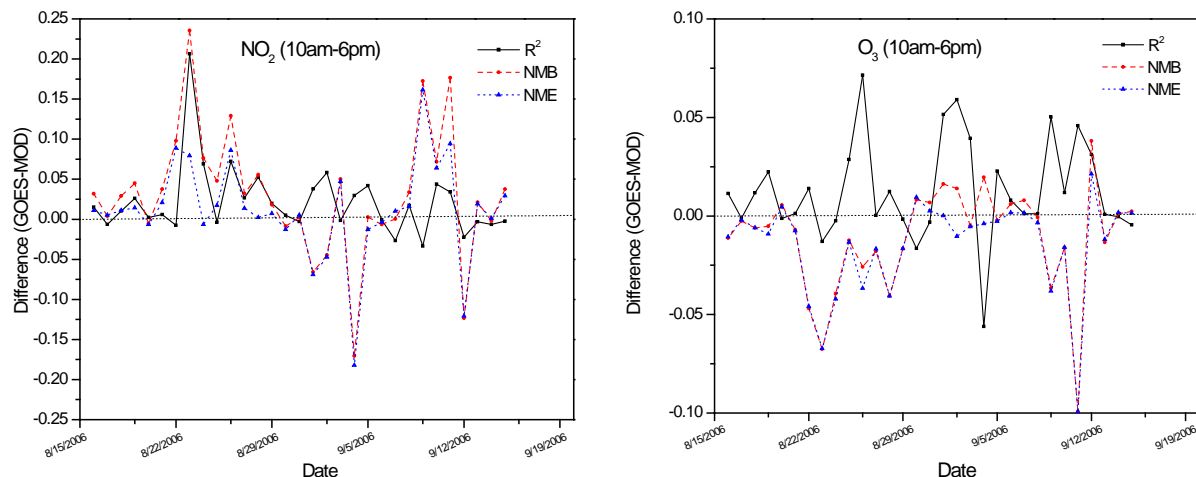


Figure 4. Change in model performance ( $R^2$ , NMB, and NME) in simulating daily 8 hours (10:00-18:00LT)  $\text{NO}_2$  (left) and  $\text{O}_3$  (right) caused by satellite-derived photolysis rates.

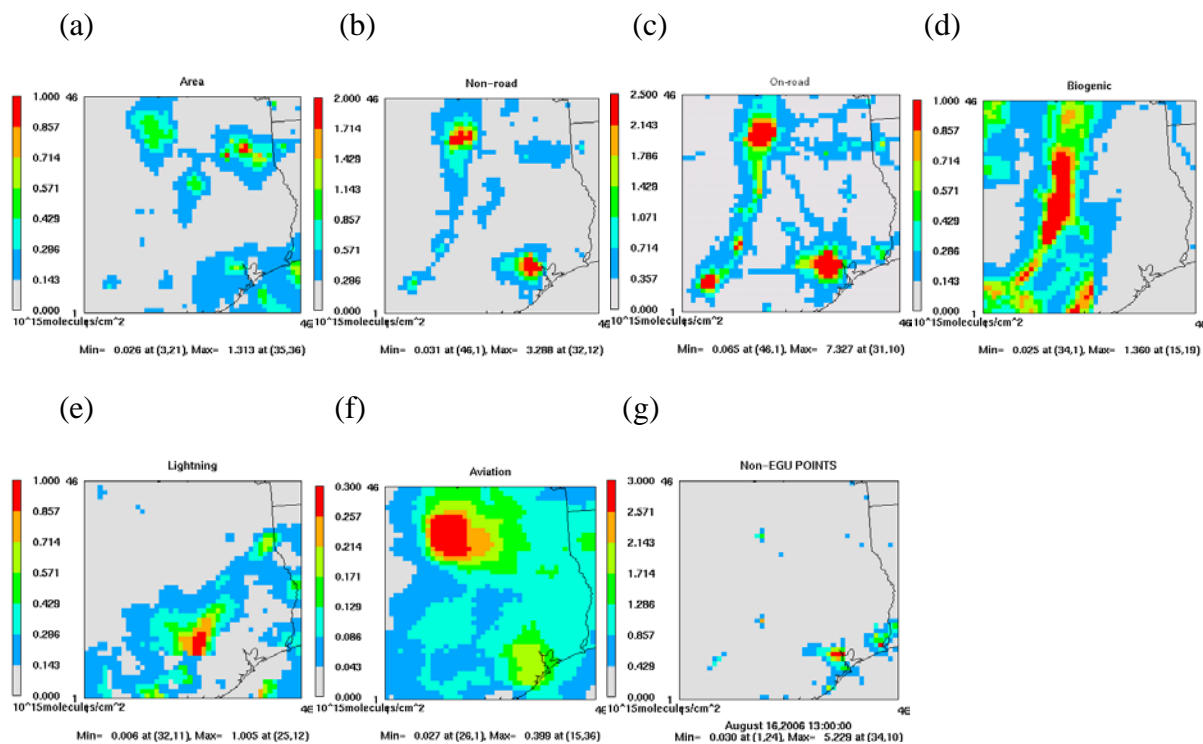


Figure 5. Vertical column densities of  $\text{NO}_2$  sensitivities to  $\text{NO}_x$  emissions of (a) area, (b) non-road, (c) on-road, (d) biogenic, (e) lightning, (f) aviation, and (g) non-EGU points source sectors.

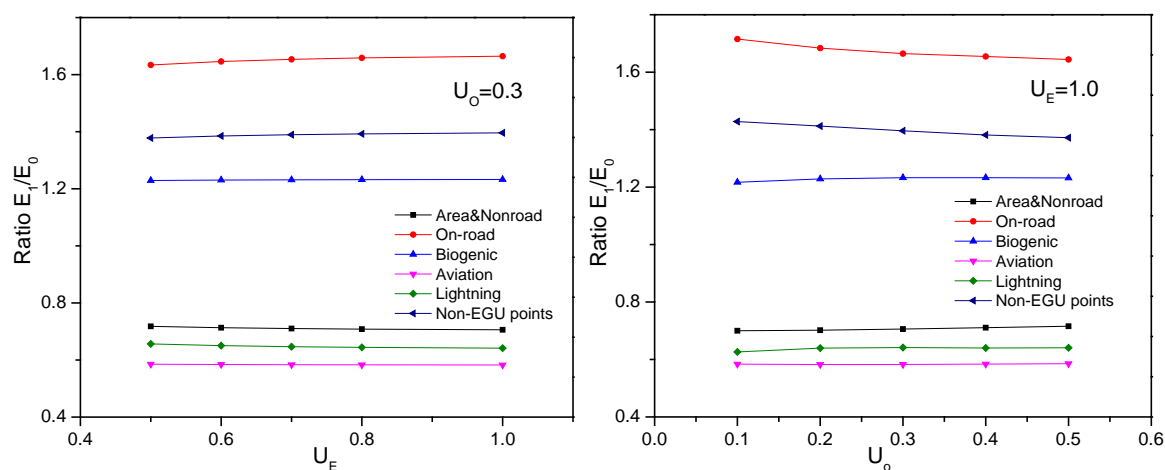
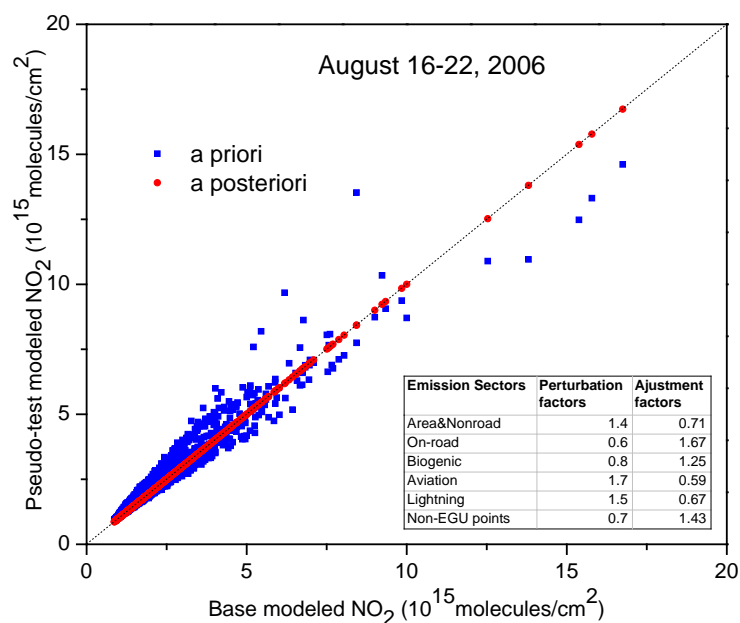


Figure 6. Pseudodata analysis for the sector-based DKF inversion (top), and its sensitivities to varied uncertainties in emissions ( $U_E$ ) (bottom left) with 30% uncertainty in observation ( $U_O$ ) and in observations (bottom right) with 100% uncertainty in emissions.

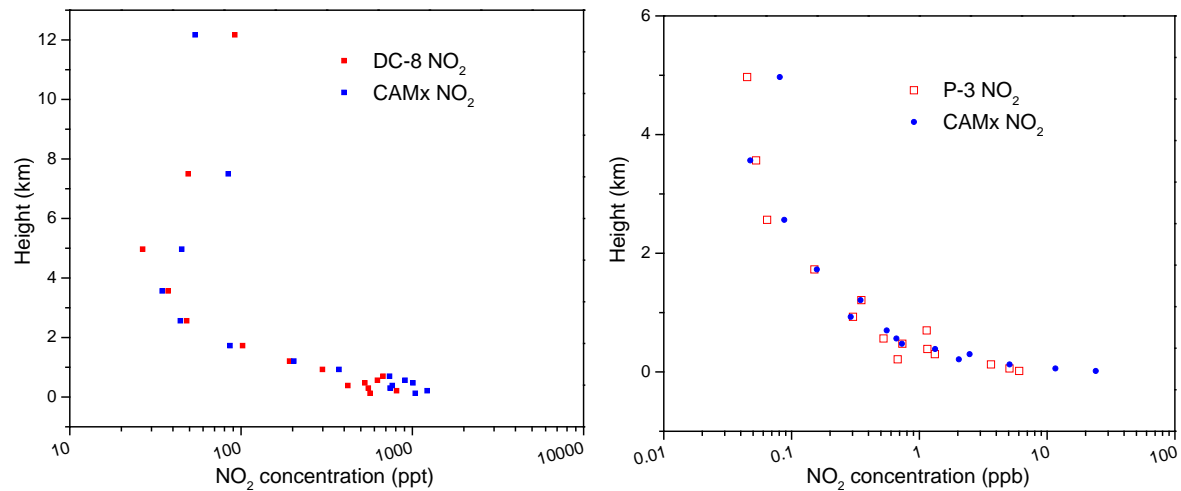


Figure 7. Comparisons of modeled NO<sub>2</sub> vertical distributions with INTEX NASA DC-8 flight (left) and TexAQS 2006 NOAA P-3 aircraft (right) measurements.



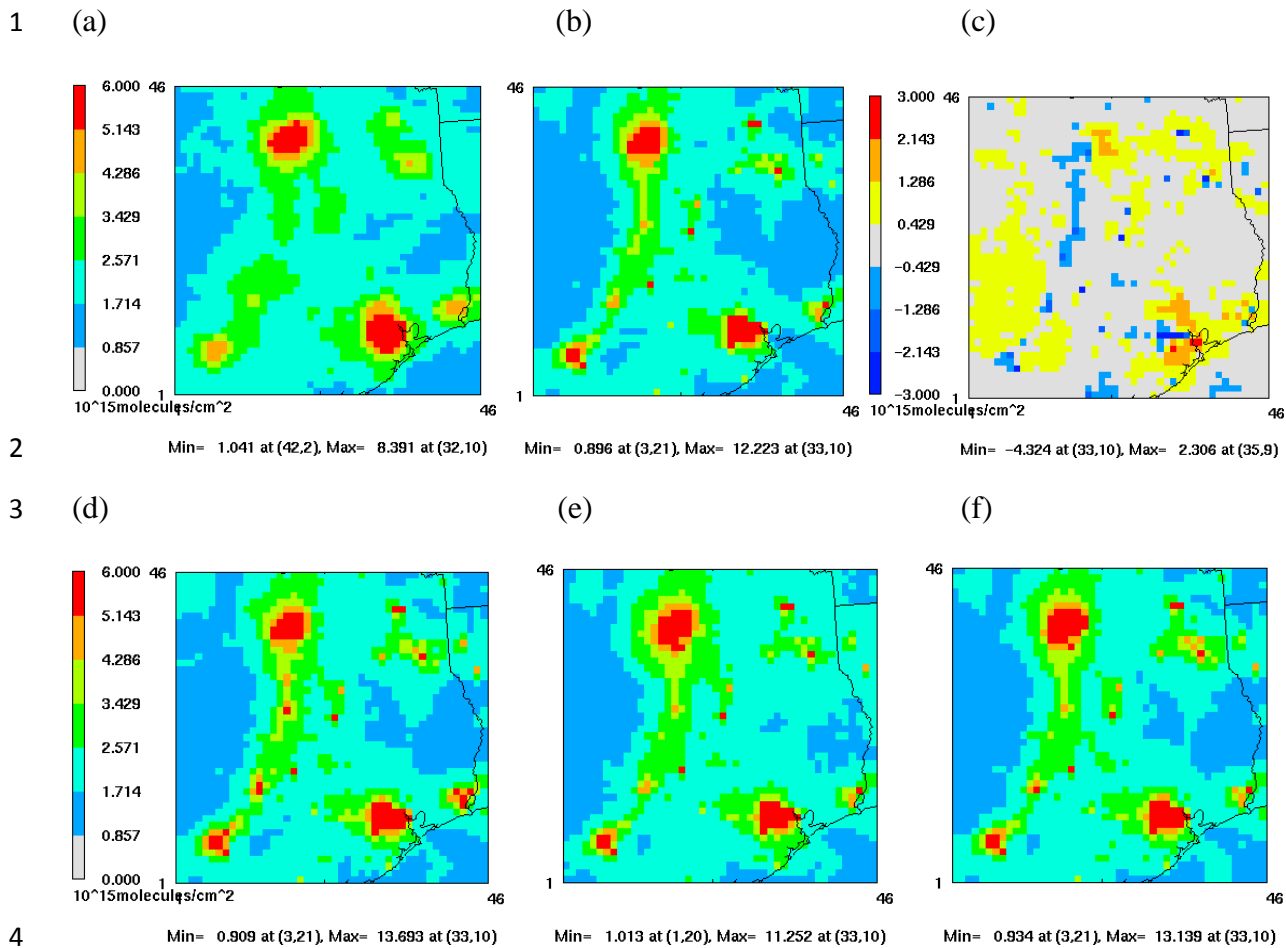


Figure 8. Monthly averaged (16 August to 15 September) tropospheric  $\text{NO}_2$  VCDs at 13:00-14:00LT from (a) OMI, (b) a priori simulation, (c) difference between OMI and a priori simulation, and simulations using a posteriori  $\text{NO}_x$  emissions generated by (d) region-based DKF inversion, and sector-based DKF inversion (e) case I and (f) case II.

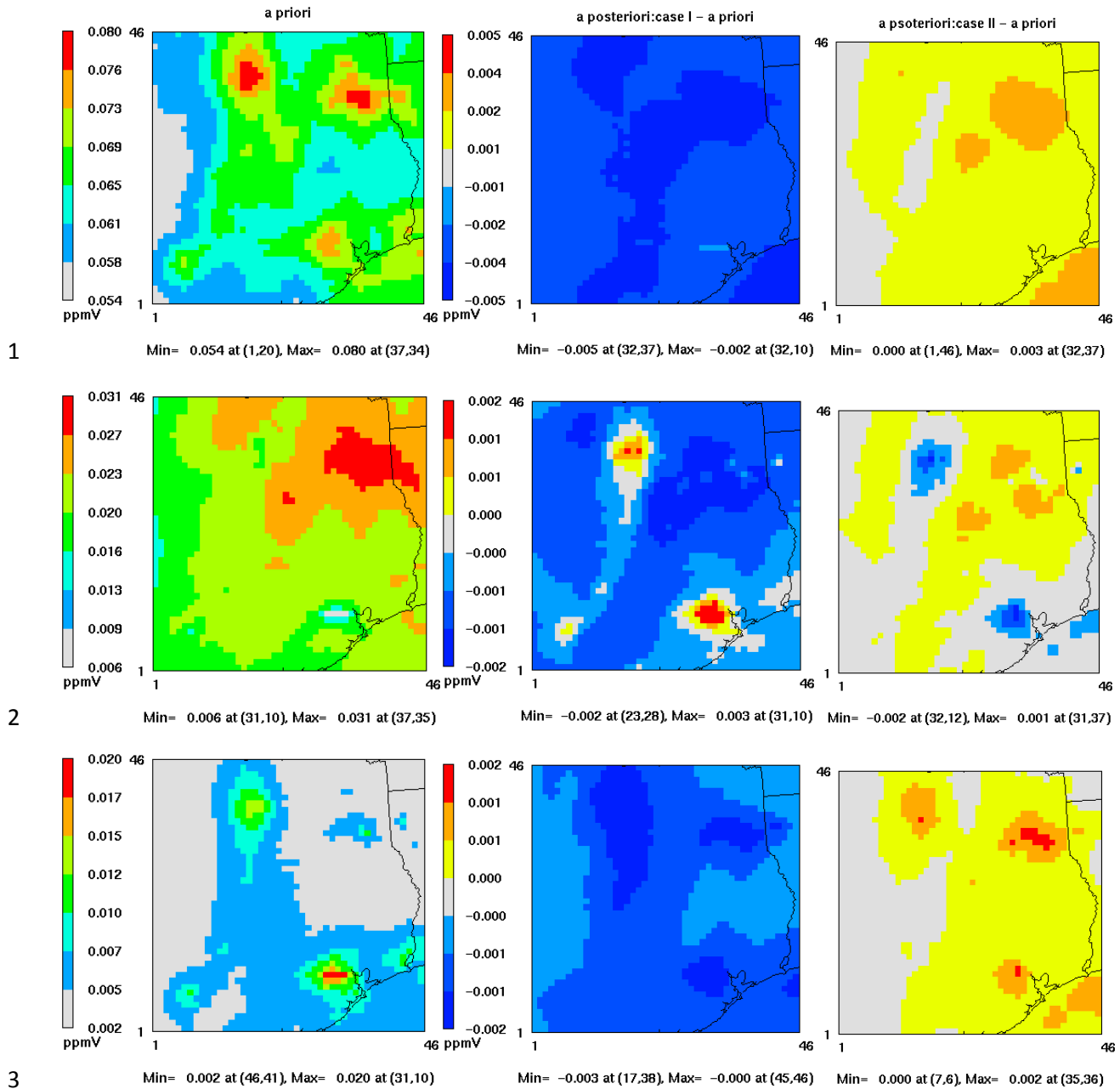


Figure 9. Monthly 8-h (10:00-18:00LT) averaged ground  $O_3$  concentrations (top),  $O_3$  sensitivity to  $NO_x$  (middle), and  $O_3$  sensitivity to VOC (bottom) for the a priori case (left), and differences between a posteriori and a priori for the sector-based DKF inversions case I (middle) and case II (right).

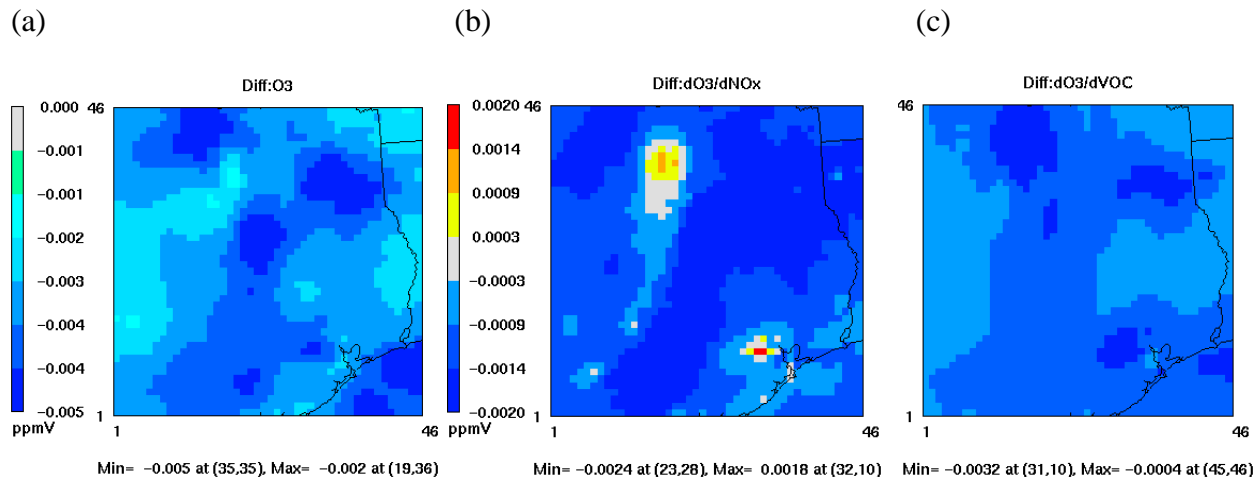


Figure 10. Monthly 8-h (10:00-18:00LT) averaged differences in modeled (a) ground O<sub>3</sub> concentrations, (b) O<sub>3</sub> sensitivity to NO<sub>x</sub>, and (c) O<sub>3</sub> sensitivity to VOC resulting from use of both satellite-derived photolysis rates and NO<sub>x</sub> emissions in place of a priori data.

## 1 Supplement

### 2 1. CAMx modeled profile-based OMI retrieval

3 The OMI-retrieved tropospheric NO<sub>2</sub> vertical column density (VCD) used in this study is  
4 calculated via Eq. (S1) (Bucsela et al., 2013),

$$5 \quad V_{c(GEOSChem)} = \frac{S_{c(OMI)}}{AMF_{GEOSChem}} \quad (S1)$$

6 where  $S_{c(OMI)}$  is the OMI tropospheric NO<sub>2</sub> slant column density,  $AMF$  stands for the air mass  
7 factor which is computed based on a priori GEOS-Chem modeled profile and scattering weights  
8 ( $SW$ ) calculated by the TOMRAD model (Bucsela et al., 2013), and  $V_{c(GEOSChem)}$  is the GEOS-  
9 Chem modeled profile-based OMI tropospheric NO<sub>2</sub> VCD. A satellite NO<sub>2</sub> retrieval error  
10 analysis study (Boersma et al., 2004) shows that the estimated a priori profile from global  
11 models may contribute approximately 10% uncertainty to the AMF calculations and propagate  
12 that uncertainty to the retrieved NO<sub>2</sub> VCD. Therefore, when OMI VCD is compared to any  
13 modeled VCD, OMI averaging kernels ( $AK_s$ ) (Eskes and Boersma, 2003), calculated in Eq. (S2),  
14 are recommended to be applied to the modeled VCD via Eq. (S3), in order to remove the  
15 influence from the a priori profile used in the OMI retrievals.

$$16 \quad AK_i = \frac{SW_i}{AMF_{GEOSChem}} \quad (S2)$$

$$17 \quad \begin{aligned} C_{NO_2}^{predicted} &= \sum(AK_i \times CAMx_{vci}) = \sum\left(\frac{SW_i}{AMF_{GEOSChem}} \times CAMx_{vci}\right) = \frac{\sum(SW_i \times CAMx_{vci})}{AMF_{GEOSChem}} \\ &= CAMx_{vctot} \times \frac{\sum(SW_i \times CAMx_{vci}) / CAMx_{vctot}}{AMF_{GEOSChem}} \end{aligned} \quad (S3)$$

1 In Eq. (S3),  $CAMx_{vci}$  represents the CAMx modeled  $NO_2$  VCD at each model layer ( $i$ ), and  
 2  $CAMx_{vctot}$  is the CAMx modeled total tropospheric VCD. The AMF which contains the a priori  
 3 GEOS-Chem modeled profile is now merged with the CAMx modeled VCD.

4 The way of removing the a priori GEOS-Chem modeled profile via applying AKs is carried  
 5 out by generating the CAMx modeled profile-based  $AMF_{CAMx}$  as shown in Eq. (S4),

$$6 \quad AMF_{CAMx} = \sum (SW_i \times \frac{CAMx_{vci}}{CAMx_{vctot}}) = \frac{\sum (SW_i \times CAMx_{vci})}{CAMx_{vctot}} \quad (S4)$$

7 using  $AMF_{CAMx}$  to replace  $AMF_{GEOSChem}$  in Eq. (S1) and then creating a CAMx modeled profile-  
 8 based OMI tropospheric  $NO_2$  VCD ( $V_{c(CAMx)}$ ). However, this procedure can only be realized in  
 9 the inversion process by comparing the AKs applied CAMx VCD ( $C_{NO_2}^{predicted}$ ) and original OMI  
 10 retrieved VCD ( $V_{c(GEOSChem)}$ ).

11 The numerator in Eq. (S3) can be replaced by the  $AMF_{CAMx}$  generated in Eq. (S4) to form Eq.  
 12 (S5).

$$13 \quad C_{NO_2}^{predicted} = CAMx_{vctot} \times \frac{AMF_{CAMx}}{AMF_{GEOSChem}} \quad (S5)$$

14 When applying  $C_{NO_2}^{predicted}$  to the direct scaling method (Martin et al., 2003; Tang et al., 2013) in Eq.  
 15 (S6),

$$16 \quad E_t = E_b \times \frac{V_{c(GEOSChem)}}{C_{NO_2}^{predicted}} = E_b \times \frac{\frac{S_{c(OMI)}}{AMF_{GEOSChem}}}{CAMx_{vctot} \times \frac{AMF_{CAMx}}{AMF_{GEOSChem}}} = E_b \times \frac{\frac{S_{c(OMI)}}{AMF_{CAMx}}}{CAMx_{vctot}} = E_b \times \frac{V_{c(CAMx)}}{CAMx_{vctot}} \quad (S6)$$

1 the  $AMF_{GEOSChem}$  is canceled out, and  $V_{c(CAMx)}$  is formed through  $AMF_{CAMx}$  to compare with the  
2 CAMx modeled VCD directly.  
3 When applying OMI AKs to the CAMx modeled  $NO_2$  and its sensitivity VCD in the DKF  
4 method (Tang et al., 2013) as shown in Eq. (S7),

$$\begin{aligned} \hat{\mathbf{x}}_{NO_x} = & \mathbf{x}_{NO_x}^- + \mathbf{P}_{NO_x}^- \times \left( \frac{AMF_{CAMx}}{AMF_{GEOSChem}} \right) \mathbf{S}_{vc}^T \times \left( \left( \frac{AMF_{CAMx}}{AMF_{GEOSChem}} \right)^2 \mathbf{S}_{vc} \mathbf{P}_{NO_x}^- \mathbf{S}_{vc}^T + \left( \frac{S_{c(OMI)}}{AMF_{GEOSChem}} \varepsilon_{OMI} \right)^2 \right)^{-1} \\ & \times \left( \left( \frac{S_{c(OMI)}}{AMF_{GEOSChem}} \right) - (CAMx_{vectot} \times \frac{AMF_{CAMx}}{AMF_{GEOSChem}}) - \left( \frac{AMF_{CAMx}}{AMF_{GEOSChem}} \right) \mathbf{S}_{vc} \mathbf{x}_{NO_x}^- \right) \end{aligned} \quad (S7)$$

6 where  $\varepsilon_{OMI}$  is the OMI measurement uncertainty, Eq. (S8) derived

$$\begin{aligned} \hat{\mathbf{x}}_{NO_x} = & \mathbf{x}_{NO_x}^- + \mathbf{P}_{NO_x}^- \times \mathbf{S}_{vc}^T \times \left( \mathbf{S}_{vc} \mathbf{P}_{NO_x}^- \mathbf{S}_{vc}^T + \left( \frac{S_{c(OMI)}}{AMF_{CAMx}} \varepsilon_{OMI} \right)^2 \right)^{-1} \\ & \times \left( \frac{AMF_{GEOSChem}}{AMF_{CAMx}} \right) \times \left( \frac{S_{c(OMI)}}{AMF_{GEOSChem}} - (CAMx_{vectot} \times \frac{AMF_{CAMx}}{AMF_{GEOSChem}}) - \left( \frac{AMF_{CAMx}}{AMF_{GEOSChem}} \right) \mathbf{S}_{vc} \mathbf{x}_{NO_x}^- \right) \end{aligned} \quad (S8)$$

8 and further transformed to Eq. (S9),

$$\hat{\mathbf{x}}_{NO_x} = \mathbf{x}_{NO_x}^- + \mathbf{P}_{NO_x}^- \times \mathbf{S}_{vc}^T \times \left( \mathbf{S}_{vc} \mathbf{P}_{NO_x}^- \mathbf{S}_{vc}^T + (V_{c(CAMx)} \varepsilon_{OMI})^2 \right)^{-1} \times (V_{c(CAMx)} - CAMx_{vectot} - \mathbf{S}_{vc} \mathbf{x}_{NO_x}^-) \quad (S9)$$

10 where all  $AMF_{GEOSChem}$  are removed, and the original  $V_{c(GEOSChem)}$  becomes  $V_{c(CAMx)}$ .

11 There is an alternative way to create  $V_{c(CAMx)}$  instead of applying OMI AKs, which is to use  
12 the CAMx modeled profile directly in the OMI retrieval process. In this case, the error of  
13 interpolating AKs values into the CAMx layer can be avoided, and the CAMx profile-based OMI  
14 retrieval can be calculated directly and viewed. In this study, we have created a CAMx profile-  
15 based OMI product that uses a CAMx profile in the retrieval process for the AMF calculation

and planned to use this new OMI retrieval product at the beginning for the inversion study. However, we find that the CAMx profile-based OMI overestimates NO<sub>2</sub> VCD by approximately 30% compared to the original OMI retrieval using a GEOS-Chem profile (Fig. S1, right). We further compare the monthly averaged 13:00-14:00LT CAMx NO<sub>2</sub> profile to the GEOS-Chem NO<sub>2</sub> profile over the 12km domain (Fig. S1 left) and find that the CAMx profile shows much higher amounts of NO<sub>2</sub> in the boundary layer but lower amounts of NO<sub>2</sub> in the upper troposphere. This may reduce the AMF values (Eq. S4) because instrument sensitivity related SW is much higher in the upper troposphere than in the boundary layer and thus increases the total retrieval quantity. Unfortunately, there are no corresponding measurement data available to validate the CAMx and GEOS-Chem profiles in Fig. (S1), but similar bias has been found in the CAMx modeled NO<sub>2</sub> profile compared to the DC-8 and P-3 aircraft NO<sub>2</sub> measurements (Fig. 8). Using the CAMx profile here may introduce more errors to the OMI retrieval and inversions; hence, we do not recommend to either apply AK to the CAMx modeled VCD or to use the CAMx profile-based OMI in this study unless the CAMx profile is validated.

## **2. Impact of increased NO<sub>x</sub> lifetime and artificial layer on modeled NO<sub>2</sub> VCDs**

The NASA OMI high resolution product used in this study shows reduced NO<sub>2</sub> in rural areas, while enhanced NO<sub>2</sub> in urban, compared to the NASA standard retrieval, version 2 (Tang et al., 2013); however, it still shows more smeared-out pattern than the CAMx modeled NO<sub>2</sub> VCDs (Fig. S3a). The CAMx simulations with the a priori NO<sub>x</sub> emission inventory created in Tang et al. (2013) shows larger NO<sub>2</sub> VCDs in the cities, while lower NO<sub>2</sub> VCDs in the rural places than OMI (Fig. S3b). Reducing the reaction rate constant of the reaction OH + NO<sub>2</sub> by 25% in the CB05 chemical mechanism increases the NO<sub>x</sub> lifetime, makes more NO<sub>x</sub> transport to rural, and enhances around 3% NO<sub>2</sub> VCDs on average in the inversion region, but the impact is small (Fig.

S3c). Implementing 40ppt NO<sub>2</sub> homogeneously into the model top layer adds about  $1.6 \times 10^{14}$  molecules.cm<sup>-1</sup> NO<sub>2</sub> densities to each model grid and increases approximately 8% NO<sub>2</sub> VCDs in the inversion region, further alleviating the NO<sub>2</sub> gap between OMI and CAMx in rural areas (Fig. S3d).

### 3. Sensitivity of DKF inversion to error covariance matrices

The sensitivities of the DKF inversion-generated scaling factors to the uncertainties in the emission and observation error covariance matrices are tested for both region-based and sector-based DKF inversions to evaluate the robustness of the inversion results (Fig. S2). The OMI observation uncertainties are fixed to 30% in the sensitivity tests for the emission error covariance matrix, while the emission uncertainties are varied from 50% to 100% (Fig. S2 left). In contrast, the OMI observation uncertainties are varied from 10% to 50% in the sensitivity tests for the observation error covariance matrix, while the emission uncertainties in each sector are fixed to 100% (Fig. S2 right). In the region-based inversion, the emission uncertainties have insignificant impact on the inversion results. The inversion seems to be relatively responsive to the lower observation uncertainties, but results become more stable when the uncertainties are over 30% (Fig. S2 top). In the sector-based inversion, the scaling factors decrease when uncertainties in the observations increase, but the inversion results are less sensitive to the emission uncertainties. However, an exception occurs in the sector-based DKF inversion case I, where the adjustments in the aviation sector are relatively more sensitive to the emission uncertainty, ranging from 3.9 to 4.6 when emission uncertainty increases from 50% to 100%. It seems to offset against area and nonroad sector which the scaling factors reduce from 0.6 to 0.5 (Fig. S2 middle). However, the inversion becomes insensitive to the emission uncertainties in the sector-based DKF inversion case II when merging aviation into the area and nonroad sector (Fig.



S2 bottom), indicating the DKF inversion in case II is more stable and less responsive to the uncertainty matrices than that in case I.

#### **4. Top-down VOC emissions**

An accurate VOC emission inventory is also important for Texas O<sub>3</sub> modeling and NO<sub>x</sub> inversion studies. The HGB and BPA regions in eastern Texas feature highly reactive VOC (HRVOC) emissions from petrochemical activities (Kleinman et al., 2002; Murphy and Allen, 2005; Nam et al., 2006; Webster et al., 2007; Vizuite et al., 2008). However, large uncertainties were found in the Texas VOC emission inventory during two intensive measurement campaigns, Texas Air Quality Study (TexAQS) 2000 and 2006, that reported HRVOC emissions were underestimated up to an order of magnitude (Ryerson et al., 2003; Wert et al., 2003; Jiang and Fast, 2004; Gilman et al., 2009; de Gouw et al., 2009; Parrish et al., 2009; Washenfelder et al., 2010). Byun et al. (2007) directly multiplied Texas HRVOC inventory values by factors of 3 to 12, and Kim et al. (2011) reconstructed HRVOC emissions in the 2005 National Emission Inventory using Solar Occultation Flux measurements, with both showing improved O<sub>3</sub> simulations over the Houston area.

In this study, five VOC species, ethylene (ETH), ethane (ETHA), isoprene (ISOP), toluene (TOL), and xylene (XYL) are chosen to conduct the inversion because of their explicit model outputs and sufficient measurement data. ETH, ISOP, TOL, and XYL are defined as highly reactive VOC (HRVOC) by TCEQ for regulatory purposes, due to their high reactivity with OH and propensity for contributing to rapid O<sub>3</sub> formation (Thomas et al., 2008). Although ETHA is not a HRVOC, the high concentrations in urban environments make it also play very important role in forming O<sub>3</sub> (Katzenstein et al., 2003; Buzcu and Fraser, 2006).

#### 4.1 Base case VOC emission inventory

The base case VOC emission inventory for the HGB SIP modeling from 13 August to 15 September 2006 was developed by TCEQ (Table S1). The non-EGU point source VOC emissions were from the State of Texas Air Reporting System (STARS) database, a special inventory containing reported hourly VOC emissions from 15 August to 15 September targeting a specific list of non-EGU points and from Tank Landing Loss surveys of hourly landing loss VOC emissions. The EGU point source VOC emissions were from the EPA Acid Rain database (ARD) with the emissions calculated based on VOC:NO<sub>x</sub> ratios. The VOC emissions from motor vehicle were generated by the Motor Vehicle Emission Simulator 2010a (MOVES2010a) model for the on-road vehicles and the Texas NONROAD (TexN) model for the off-road vehicles. The VOC emissions from the other non-road and area sources were from the Texas Air Emissions Repository (TexAER) database (TCEQ 2010). The Global Biosphere Emissions and Interactions System model, version 3.1 (GloBEIS3.1) was used for developing biogenic VOC emissions (Yarwood et al., 1999). Four HRVOC species emissions, ethylene, propylene, 1,3-butadiene, and butenes were further corrected using the Potential Source Contribution Function (PSCF) technique with Automatic Gas Chromatographs (Auto-GC) measured data in the HGB area (TCEQ 2010).

For the five chosen VOC species, ETH and ISOP emissions are mostly contributed by the biogenic source around 60% and 99%, respectively, while TOL and XYL are entirely anthropogenic, originating mostly from area emissions. Area sources also dominate emissions of ETHA, which does not appear in the on-road mobile source. EGUs emissions are minor contributors to all five VOC species (Table S1).

## 4.2 VOC observations

The U.S. EPA Photochemical Assessment Monitoring Stations (PAMS) VOC measurement data (<http://www.epa.gov/ttn/airs/airsaqs/>) are used here to adjust emissions for the five chosen VOC species. All five VOC species were measured by the gas chromatographs-flame ionization detector (GC-FID) with 1-hr resolution for the entire modeling period from 13 August to 15 September 2006 in the unit of ppmC (U.S. EPA 1998). Measurements are available only for a total of 11 PAMS monitoring sites in the inversion region: 2 in DFW, 3 in BPA and 6 in HGB (Fig 1). The measurement data are first converted into the unit of ppb for each VOC species, and then averaged monthly over all monitoring sites in each region and compared to the corresponding modeled data.

The NOAA P-3 aircraft measured VOC data (<http://www.esrl.noaa.gov/csd/tropchem/2006TexAQS/>) are further used for evaluating the model performance in simulating aloft VOCs. Only four chosen VOC species, ETH, ISOP, TOL, and XYL are measured by P-3. ETH is measured using Laser Photoacoustic Spectroscopy (LPAS) with 20s resolution (de Gouw et al., 2009), and ISOP, TOL, and XYL are measured using Proton Transfer Reaction Mass Spectrometer (PTRMS) with 15s resolution (de Gouw et al., 2003). The P-3 measured ISOP, TOL, and XYL are available on 4 days (31 August, 11 September, 13 September, and 15 September 2006), while measured ETH is only available on 3 days (31 August, 13 September, and 15 September 2006) during our modeling period. The P-3 measured VOC data are averaged hourly and compared with the hourly modeled data at corresponding grid cells.

### 4.3 Results

Since all modeled ETH, ETHA, ISOP, TOL, and XYL are from the primary emissions, a direct scaling (DS) inversion method that adjusts VOC emissions based on the ratios between modeled VOC and PAMS measured VOC is applied here. The inversion is conducted on a regional basis, which means the scaling factor calculated from the measurement data in one region only applies to adjust the emissions in that region. Therefore, due to the availability of observations, the five chosen VOC species emissions are adjusted in only three regions, DFW, HGB, and BPA.

The scaling factors generated from the inversions vary significantly in different regions (Table S2) and show that the HRVOC emissions in the 2006 TCEQ emission inventory for HGB SIP modeling are much better than the reported uncertainty of an order of magnitude (Ryerson et al., 2003; Parrish et al., 2009) but still much higher than the uncertainty in NO<sub>x</sub> emissions. The ETHA emissions require the largest adjustments in all three regions with scaling factors ranging from 3.14 to 4.63. The inversion scales down ETH emissions in the HGB and DFW regions by only 10%, but in BPA, it requires a scaling factor of 3.33. The mostly biogenic source contributed ISOP emission only requires 4% scale-up adjustment in HGB, but relatively larger scale-down adjustments ranging from 30-50% in DFW and BPA. The anthropogenic source contributed TOL emissions require scale-up adjustments in all three regions by scaling factors ranging from 1.32 to 2.22. The XYL emissions are well estimated in the base case emission inventory for the HGB region, but require scale-down by approximately 70% in DFW and scale-up around 50% in BPA.

The temporal variations of the five VOC species (Fig.S4) show that the discrepancies between observed VOCs and the a priori modeled VOCs are significantly reduced by using the a posteriori emissions. The inverted ETHA emission improves modeled R<sup>2</sup> and reduces modeled

1 NMB and NME by 0.5 and 0.1, respectively (Table S3). The inversed ETH shows increased  $R^2$   
2 and 0.13 reduced NMB, but no improvement in the modeled NME against ground measurement  
3 (Table S3); however, it shows 0.4 reductions in both modeled NMB and NME against P-3  
4 measured data (Table S4). The inverted ISOP emissions reduce approximately 20% NMB and  
5 NME in ground ISOP simulation (Table S3), but no improvements are found compared against  
6 aircraft measurement (Table S4). The modeled NMB in the inversed TOL is reduced by  
7 approximately 0.4 (Table S3) compared against PAMS and 0.13 compared against P-3 (Table  
8 S4), while the modeled NME has not been improved. The inversed XYL shows increased  $R^2$  and  
9 around 0.2 reduced modeled NMB and NME compared to ground measurement (Table S3) and  
10 0.02 reduced modeled NMB and NME compared to aircraft measurement (Table S4). However,  
11 no improvements are found in the model performance of simulating ground-level  $\text{NO}_2$  (Table S5),  
12 and there is a slight decreasing, around 0.01, of modeled NMB and NME in ground-level  $\text{O}_3$   
13 simulations using the inverted VOC emissions (Table S6).

## References

- Boersma, K. F., Eskes, H. J., and Brinksma, E. J.: Error analysis for tropospheric NO<sub>2</sub> retrieval from space. *J. Geophys. Res.*, 109, D04311, doi:10.1029/2003JD003962, 2004.
- Bucsela, E. J., Krotkov, N. A., Celarier, E. A., Lamsal, L. N., Swartz, W. H., Bhartia, P. K., Boersma, K. F., Veefkind, J. P., Gleason, J. F., and Pickering, K. E.: A new stratospheric and tropospheric NO<sub>2</sub> retrieval algorithm for nadir-viewing satellite instruments: applications to OMI. *Atmos. Meas. Tech.*, 6, 2607–2626, 2013.
- Buzcu, B and Fraser, M. P.: Source identification and apportionment of volatile organic compounds in Houston, TX. *Atmos. Environ.*, 40, 2385–2400, 2006.
- Byun, D. W., Kim, S-T., and Kim, S. B.: Evaluation of air quality models for the simulation of a high ozone episode in the Houston metropolitan area. *Atmos. Environ.*, 41, 837–853, 2007.
- de Gouw, J., Warneke, C., Karl, T., Eerdekens, G., van der Veen, C., and Fall, R.: Sensitivity and specificity of atmospheric trace gas detection by proton-transfer-reaction mass spectrometry. *Int. J. Mass. Spectrom.*, 223– 224, 365–382, 2003.
- de Gouw, J. A., Te Lintel Hekkert, S., Mellqvist, J., Warneke, C., Atlas, E. L., Fehsenfeld, F. C., Fried, A., Frost, G. J., Harren, F. J. M., Holloway, J. S., Lefer, B., Lueb, R., Meagher, J. F., Parrish, D. D., Patel, M., Pope, L., Richter, D., Rivera, C., Ryerson, T. B., Samuelsson, J., Walega, J., Washenfelder, R. A., Weibring, P., and Zhu, X.: Airborne measurements of ethane from industrial sources using laser photo-acoustic spectroscopy. *Environ. Sci. Technol.*, 43, 2437–2442, 2009.
- Eskes, H. J. and Boersma, K. F.: Averaging kernels for DOAS total column satellite retrievals. *Atmos. Chem. Phys.*, 3, 1285–1291, 2003.
- Gilman, J. B., Kuster, W. C., Goldan, P. D., Herndon, S. C., Zahniser, M. S., Tucker, S. C., Brewer, W. A., Lerner, B. M., Williams, E. J., Harley, R. A., Fehsenfeld, F. C., Warneke, C., and de Gouw, J. A.: Measurements of volatile organic compounds during the 2006 TexAQS/GoMACCS campaign: Industrial influences, regional characteristics, and diurnal dependencies of the OH reactivity. *J. Geophys. Res.*, 114, D00F06, doi:10.1029/2008JD011525, 2009.
- Jiang, G. and Fast, J. D.: Modeling the effects of VOC and NO<sub>x</sub> emission sources on ozone formation in Houston during the TexAQS 2000 field campaign. *Atmos. Environ.*, 38, 5071–5085, 2004.
- Katzenstein, A. S., Doeze, L. A., Simpson, I. J., Blake, D. R., and Sherwood Rowland, F.: Extensive regional atmospheric hydrocarbon pollution in the southwestern United States. *Proc Natl Acad Sci.*, 100, 11975–11979, 2003.
- Kim, S. W., McKeen, S. A., Frost, G. J., Lee, S.-H., Trainer, M., Richter, A., Angevine, W.M., Atlas, E., Bianco, L., Boersma, K. F., Brioude, J., Burrows, J. P., de Gouw, J., Fried, A., Gleason, J., Hilboll, A., Mellqvist, J., Peischl, J., Richter, D., Rivera, C., Ryerson, T., te Lintel Hekkert, S., Walega, J., Warneke, C., Weibring, P., and Williams, E.: Evaluations of NO<sub>x</sub> and highly reactive VOC emission inventories in Texas and their implications for ozone plume simulations during the Texas Air Quality Study 2006. *Atmos. Chem. Phys.*, 11, 11361–11386, 2011.
- Kleinman, L. I., Daum, P. H., Imre, D., Lee, Y.-N., Nunnemacker, L. J., and Springston, S.R.: Ozone production rate and hydrocarbon reactivity in five urban areas: A case of high ozone concentration in Houston. *Geophys. Res. Lett.*, 29, 1467 10.1029/2001GL014569, 2002.

- 1 Martin, R. V., Jacob, D. J., Chance, K., Kurosu, T. P., Palmer, P. I., and Evans, M. J.:  
2 Global inventory of nitrogen oxide emissions constrained by space-based observations of  
3 NO<sub>2</sub> columns. *J. Geophys. Res.*, 108(D17), 4537, doi:10.1029/2003JD003453, 2003.
- 4 Murphy, C. F. and Allen, D. T.: Hydrocarbon emissions from industrial release events in the  
5 Houston-Galveston area and their impact on ozone formation. *Atmos. Environ.*, 39, 3785–  
6 3798, 2005.
- 7 Nam, J., Kimura, Y., Vizuete, W., Murphy, C., and Allen, D. T.: Modeling the impacts of  
8 emission events on ozone formation in Houston, Texas. *Atmos. Environ.*, 40, 5329–5341,  
9 2006.
- 10 Parrish, D. D., Allen, D. T., Bates, T. S., Estes, M., Fehsenfeld, F. C., Feingold, G., Ferrare, R.,  
11 Hardesty, R. M., Meagher, J. F., Nielsen-Gammon, J. W., Pierce, R. B., Ryserson, T. B.,  
12 Seinfeld, J. H., and Williams, E. J.: Overview of the second Texas Air Quality Study  
13 (TexAQs II) and the Gulf of Mexico Atmosphere Composition and Climate Study  
14 (GoMACCS). *J. Geophys. Res.*, 114, D00F13, doi: 10.1029/2009JD011842, 2009.
- 15 Ryerson, T. B., Trainer, M., Angevine, W. M., Brock, C. A., Dissly, R. W., Fehsenfeld, F. C.,  
16 Frost, G. J., Goldan, P. D., Holloway, J. S., Hubler, G., Jakoubek, R. O., Kuster, W. C.,  
17 Neuman, J. A., Nicks Jr., D. K., Parrish, D. D., Roberts, J. M., and Sueper, D. T.: Effect of  
18 petrochemical industrial emissions of reactive alkenes and NO<sub>x</sub> on tropospheric ozone  
19 formation in Houston, Texas. *J. Geophys. Res.*, 108 D084249, doi:10.1029/2002JD003070,  
20 2003.
- 21 Tang, W., Cohan, D. S., Lamsal, L.N., Xiao, X., and Zhou, W.: Inverse modeling of Texas NO<sub>x</sub>  
22 Emissions using space-based and ground-based NO<sub>2</sub> observations. *Atmos. Chem. Phys.*, 13,  
23 11005-11018, 2013.
- 24 TCEQ.: Houston-Galveston-Brazoria Attainment Demonstration SIP Revision for the 1997  
25 Eight-Hour Ozone Standard, Austin, TX, 2010.
- 26 Thomas, R., Smith, J., Jones, M., MacKay, J., and Jarvie, J. Emissions Modeling of Specific  
27 Highly Reactive Volatile Organic Compounds (HRVOC) in the Houston-Galveston-  
28 Brazoria Ozone Nonattainment Area. TCEQ, Austin, TX, 2008.
- 29 U.S. EPA.: Technical Assistance Document for Sampling and Analysis of Ozone Precursors.  
30 U.S. EPA, Research Triangle Park, N.C. EPA/600-R-98/161., 1998.
- 31 Vizuete, W., Kim, B.-U., Jeffries, H., Kimura, Y., Allen, D. T., Kioumourtoglou, M. A.,  
32 Biton, L., and Henderson, B.: Modeling ozone formation from industrial emission events in  
33 Houston, Texas. *Atmos. Environ.*, 42, 7641–7650, 2008.
- 34 Washenfelder, R. A., Trainer, M., Frost, G. J., Ryerson, T. B., Atlas, E. L., de Gouw, J. A.,  
35 Flocke, F. M., Fried, A., Holloway, J. S., Parrish, D. D., Peischl, J., Richter, D.,  
36 Schauffler, S. M., Walega, J. G., Warneke, C., Weibring, P., and Zheng, W.:  
37 Characterization of NO<sub>x</sub>, SO<sub>2</sub>, ethane, and propene from industrial emission sources in  
38 Houston, Texas. *J. Geophys. Res.*, 115, D16311, doi:10.1029/2009JD013645, 2010.
- 39 Webster, M., Nam, J., Kimura, Y., Jeffries, H., Vizuete, W., and Allen, D. T.: The effect of  
40 variability in industrial emissions on ozone formation in Houston, Texas.  
41 *Atmos. Environ.*, 41, 9580–9593, 2007.
- 42 Wert, B. P., Trainer, M., Fried, A., Ryerson, T. B., Henry, B., Potter, W., Angevine, W. M.,  
43 Atlas, E., Donnelly, S. G., Fehsenfeld, F. C., Frost, G. J., Goldan, P. D., Hansel, A.,  
44 Holloway, J. S., Hubler, G., Kuster, W. C., Nicks Jr., D. K., Neuman, J. A., Parrish, D. D.,  
45 Schauffler, S., Stutz, J., Sueper, D. T., Wiedinmyer, C., Wisthaler, A., Signatures of

1 terminal alkene oxidation in airborne formaldehyde measurements during TexAQS 2000. J.  
2 Geophys. Res., 108, 4104, doi:10.1029/2002JD002502, 2003.  
3 Yarwood, G., Wilson, G., Emery C., and Guenther, A.: Development of the GloBEIS—a state of  
4 the science biogenic emissions modeling system. Final Report to the Texas Natural  
5 Resource Conservation Commission., Austin, TX., 1999.  
6



1 Table S1. Emission rates of five VOC species for six emission sectors in the inversion region  
2 (tons/day).

VOCs	Area	On-road	Non-road	Biogenic	Non-EGU points	EGU points	Total
ETH	19.2 (11.5%)	14.9 (8.9%)	11.1 (6.6%)	104.8 (62.6%)	17.2 (10.3%)	0.1 (0.06%)	167.3
ETHA	232.4 (82.3%)	0 (0%)	5 (1.8%)	22.5 (8.0%)	20.4 (7.2%)	2.1 (0.7%)	282.4
ISOP	0.4 (0.002%)	0.8 (0.005%)	0.5 (0.003%)	15835.8 (99.9%)	0.2 (0.001%)	0 (0%)	15837.9
TOL	53.3 (48.9%)	24.5 (22.5%)	25.1 (23.1%)	0 (0%)	5.3 (4.9%)	0.7 (0.6%)	108.9
XYL	116.7 (58.3%)	38.2 (19.1%)	39.7 (19.8%)	0 (0%)	3.3 (1.6%)	2.2 (1.1%)	200.1

3 Note: percentage indicates the apportionment of each emission sector to the regional total.

4

5 Table S2. Direct scaling factors for VOC species in three inversion regions.

Source Region	A priori (tons/day)					Direct Scaling factors relative to a priori (unitless)				
	ETHA	ETH	ISOP	TOL	XYL	ETHA	ETH	ISOP	TOL	XYL
HGB	52.7	26.4	635.5	23.9	42.1	3.45	0.92	1.04	1.71	0.98
DFW	14.3	11.5	780.5	20.6	45.1	4.63	0.90	0.71	1.32	0.33
BPA	27.6	7.1	282.2	5.7	6.9	3.14	3.33	0.50	2.22	1.47

6

7 Table S3. Evaluation of CAMx modeled VOCs using hourly PAMS-measured VOCs.

Source Region	Priori					Posteriori				
	ETHA	ETH	ISOP	TOL	XYL	ETHA	ETH	ISOP	TOL	XYL
R <sup>2</sup>	0.12	0.05	0.04	0.09	0.07	0.13	0.10	0.04	0.09	0.12
NMB	-0.71	-0.20	0.32	-0.41	0.24	-0.22	-0.07	0.05	-0.03	0.01
NME	0.73	0.80	1.04	0.63	0.90	0.61	0.81	0.86	0.69	0.69

8

9

1 Table S4. Evaluation of CAMx modeled VOCs using P-3 aircraft-measured VOCs<sup>a</sup>.

Source Region	Priori				Posteriori			
	ETH <sup>b</sup>	ISOP	TOL	XYL <sup>c</sup>	ETH	ISOP	TOL	XYL
NMB	-0.63	-0.81	-0.60	-0.53	-0.59	-0.81	-0.47	-0.51
NME	0.84	1.05	0.72	0.80	0.80	1.05	0.72	0.78

2 a. Comparison available for four days (31 August, 11 September, 13 September, and 15 September 2006).

3 b. Comparison only available for three days (31 August, 13 September, and 15 September 2006).

4 c. Compared with measured C-8 aromatics

6 Table S5. Evaluation of CAMx modeled NO<sub>2</sub> using hourly AQS ground-measured NO<sub>2</sub>.

Source Region	Priori			Posteriori		
	R <sup>2</sup>	NMB	NME	R <sup>2</sup>	NMB	NME
HGB	0.51	0.46	0.67	0.51	0.46	0.67
DFW	0.49	0.43	0.66	0.49	0.43	0.66
BPA	0.45	0.92	1.02	0.45	0.92	1.02
Overall	0.51	0.51	0.72	0.51	0.51	0.73

8 Table S6. Evaluation of CAMx modeled O<sub>3</sub> using hourly AQS ground-measured O<sub>3</sub>.

Source Region	Priori			Posteriori		
	R <sup>2</sup>	NMB	NME	R <sup>2</sup>	NMB	NME
HGB	0.46	0.68	0.75	0.46	0.68	0.75
DFW	0.64	0.21	0.32	0.64	0.20	0.31
BPA	0.47	0.66	0.70	0.46	0.65	0.69
Overall	0.50	0.42	0.50	0.50	0.41	0.49

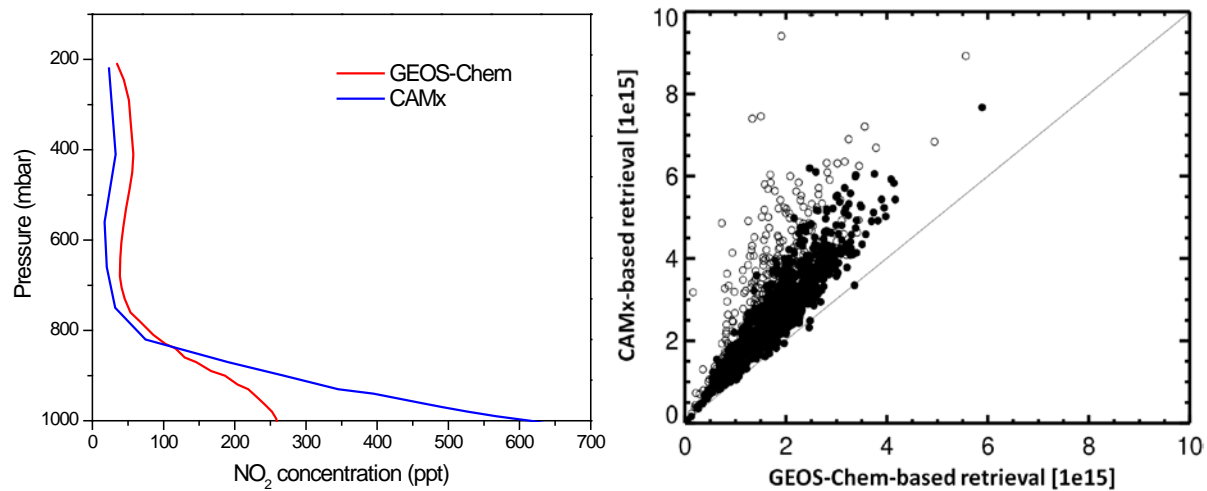


Figure S1. Comparisons between GEOS-Chem and CAMx modeled NO<sub>2</sub> vertical profiles (left) and corresponded OMI retrievals (right). Filled circles represent observations under clear sky condition (cloud fraction <0.5), and open circles are all observations.

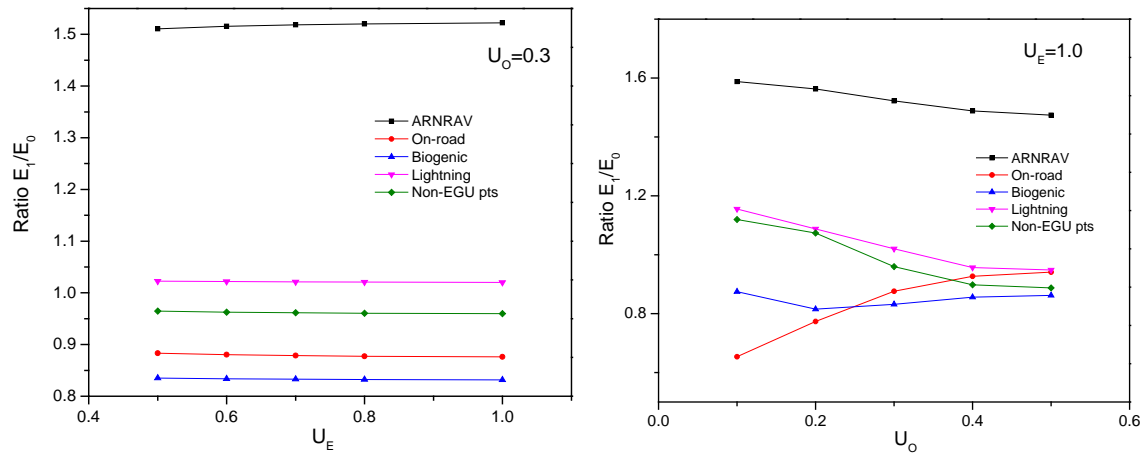
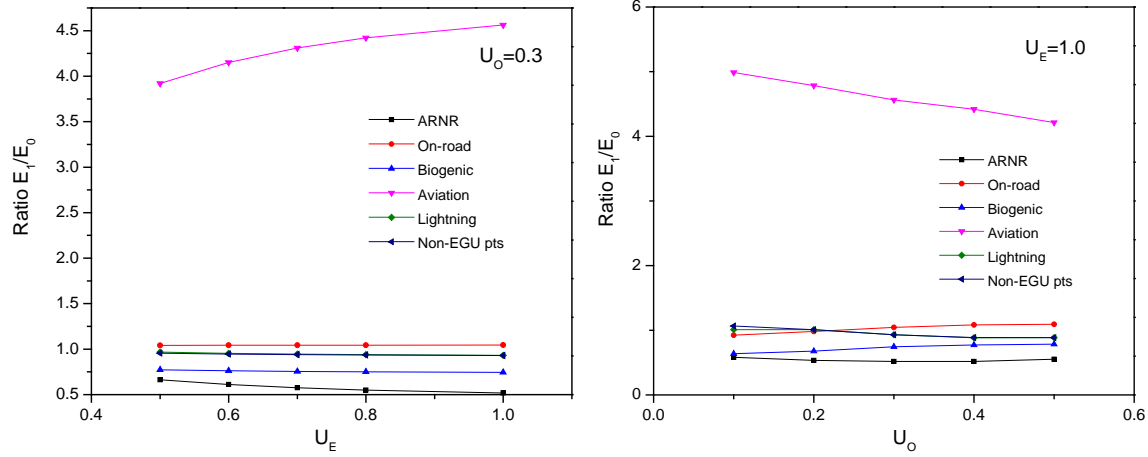
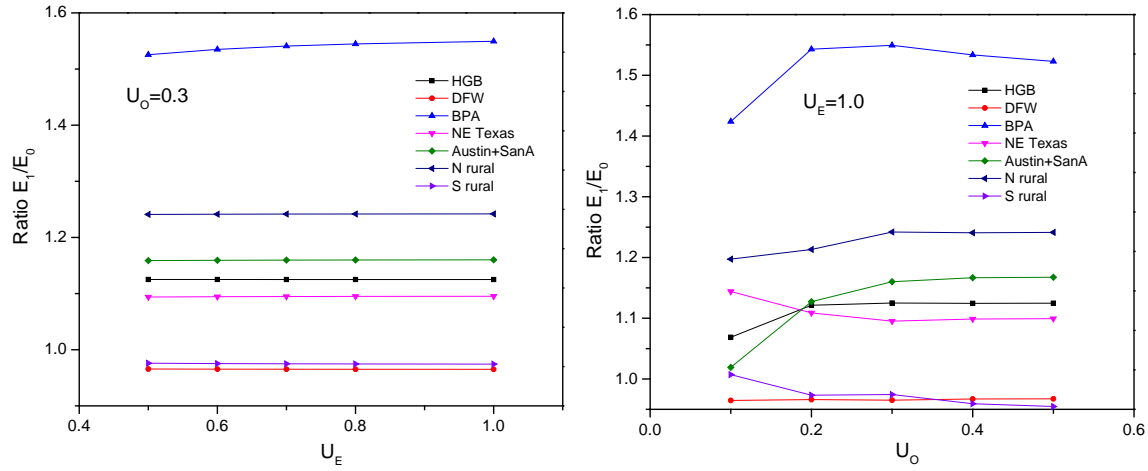


Figure S2. Sensitivities of the DKF inversions to the uncertainties in emissions (left) and in OMI observations (right) in region-based inversion (top), sector-based inversion case I (middle), and sector-based inversion case II (bottom).

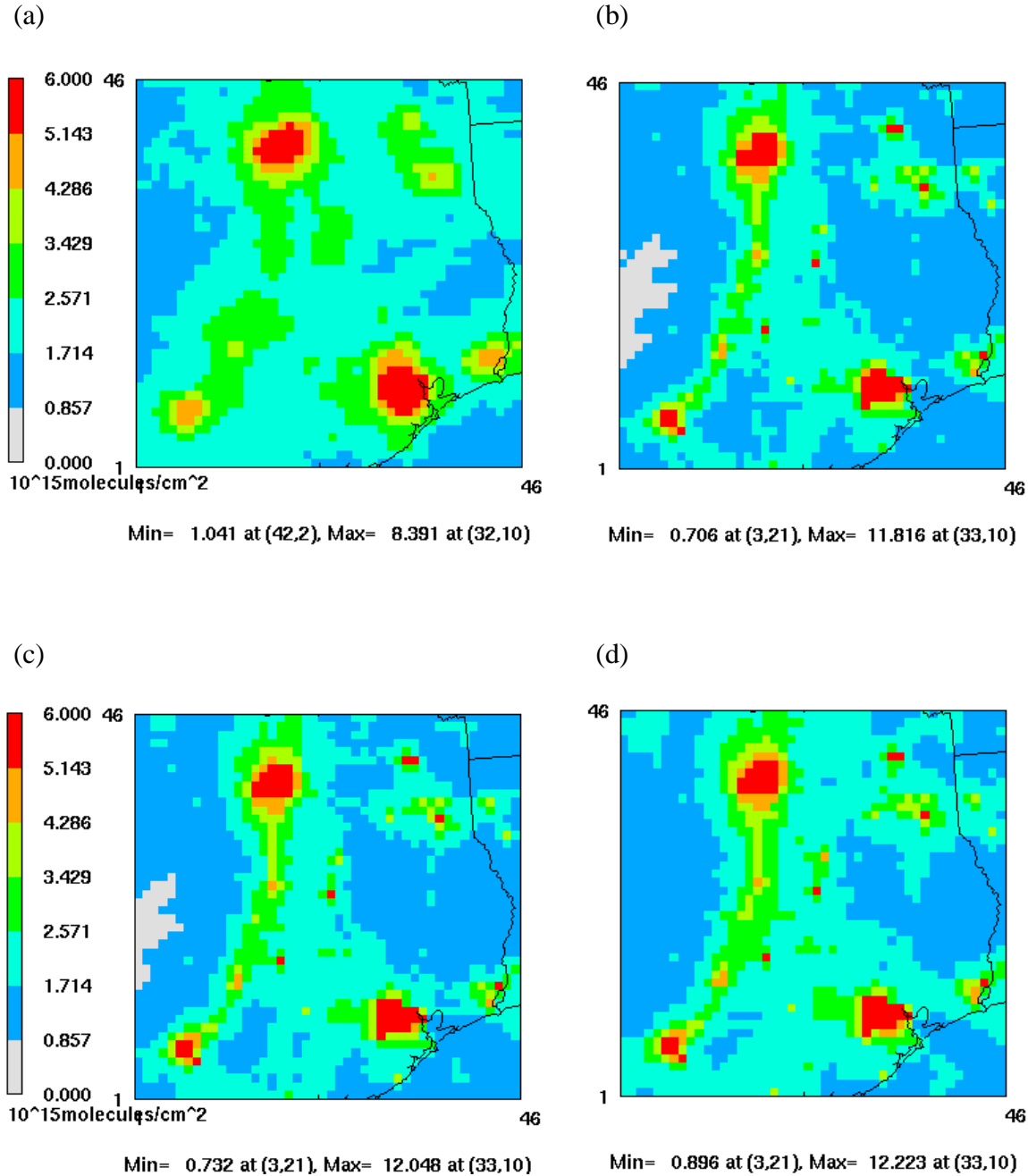


Figure S3. Monthly averaged (16 August to 15 September) tropospheric NO<sub>2</sub> VCDs at 13:00-14:00LT from (a) OMI, (b) simulations using NO<sub>x</sub> emissions from Tang et al., (2013), (c) simulations with the lower rate constant of the reaction OH+NO<sub>2</sub> from (b), and (d) simulations with added 40ppt NO<sub>2</sub> layer from (c).

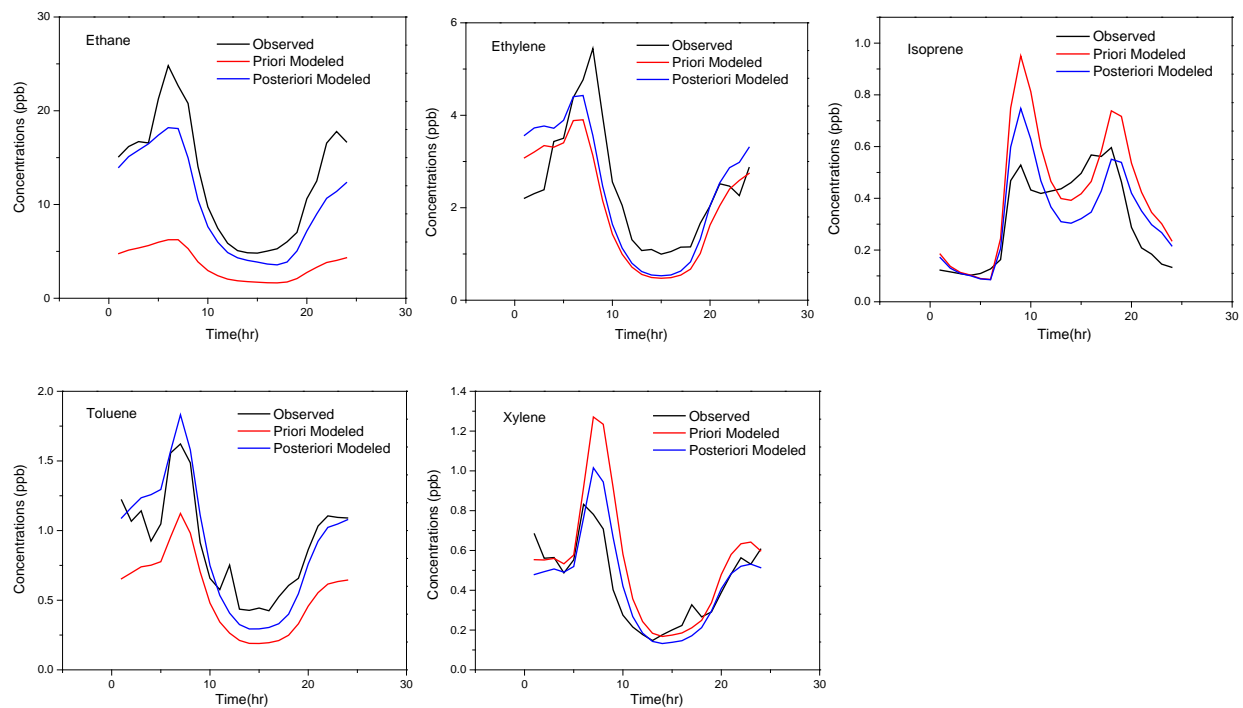


Figure S4. Comparisons of monthly averaged daily variation between observed (black) and modeled VOC species using the a priori (red) and the a posteriori (blue) VOC emission inventory over all monitoring sites.